Atomic Force Microscopy Study of Model Lipid Monolayers

by

Tamara Rozina

A thesis
presented to the University of Waterloo
in fulfillment of the
thesis requirement for the degree of
Master of Science
in
Physics

Waterloo, Ontario, Canada, 2012

I hereby declare that I am the sole author of this thesis. This is a true copy of the thesis, including any required final revisions, as accepted by my examiners.

I understand that my thesis may be made electronically available to the public.

Abstract

Alzheimer's Disease (AD) is a neurodegenerative disorder that is prevalent among the elderly population. Aβ protein has been heavily implicated in the pathogenesis of AD. This protein in its fibrillar form is a major component in the senile plaques that form on neuronal cellular membranes during the course of AD. Despite substantial efforts the exact mechanism of Aβ toxicity towards a cell membrane is not well-understood. The determination of this mechanism, however, is of utmost importance, since the membrane presents the first site of Aβ interaction with neurons, which in turn maybe the origin of Aβ neurotoxicity. The purpose of this study was to find a lipid composition that can be used as a model of neuronal membrane for subsequent studies of the role of topographical heterogeneity (domain formation) on Aβ-membrane interaction as related to AD. The lipids used in the study were 1-palmitoyl-2-oleoyl-sn-glycero-3-phosphocholine (POPC), 1-palmitoyl-2-oleoyl-sn-glycero-3-phosphoglycerol (POPG), cholesterol (Chol), sphingomyelin (SM) and ganglioside GM1 (GM1). These lipids were combined in different proportions and deposited on a mica substrate to form supported monolayers. They were then imaged with an atomic force microscope (AFM) to determine if any of them exhibited domain formation. Three of the studied samples: POPC/POPG/SM 40:40:20 +5%Chol, POPC/SM/Chol 75:20:5 and POPC/SM/GM1/Chol 74:2:1:23 were found to possess interesting topography, rich in structural features: pores and domains. The average height difference between the domain features for each sample was found to be 0.58 ± 0.15 nm, 0.61 ± 0.12 nm and 0.27 ± 0.07 nm.

Acknowledgments

I would like to thank my supervisor, Dr. Zoya Leonenko for the wonderful opportunity she gave me. I am deeply grateful for the guidance and encouragement I received from her. Zoya's concern for the success and well being of her students is truly inspiring.

I would also like to thank the other members of the Leonenko Lab. I thank Dr. Ravi Gaikwad for his unending patience in teaching me how to use the AFM. I learned so much from him about its theoretical aspects and practical applications. Ravi also taught me how to use SPIP software for my data analysis, which saved me a lot of time and confusion. I thank Liz Drolle for teaching me how to prepare and store my samples. Liz's instruction on the use of the L-B trough was invaluable. Special thank you to Martin Loskill, a visiting student, who helped me with the literature search in preparation for the fluorescence experiments. Even though in the end the experiments never happened it was great to have Martin's input and I'm very grateful for the effort he put into his work. Many thanks to Robbie Henderson for all his good advice and for teaching me a little bit about statistics.

Additional thanks to Dr. Simon Attwood for insight and advice on data analysis, to Vince Choi for always willing to help and answer questions, to Brenda Lee for taking care of so many administrative tasks, to Nancy Elewa for taking care of accommodations for the ISPM tutorial, to Steven Cheung for making AFM training fun rather than daunting, and to Tavo Cordova for sharing thesis-writing tips.

I had a lot of great experiences during my time in the Leonenko Lab. I'm truly grateful for the warm and friendly atmosphere in the group. Everyone was extremely helpful and patient and I owe them a deep debt of gratitude. THANK YOU!!!

Dedication

I dedicate this thesis to my family and friends:

To my mother, who has been my steadfast rock over the years of my studies, who supported me, comforted me, believed in me, and gave me strength. I'm sorry for all the gray hairs that must've given you. I don't know what I would've done if you weren't there for me.

To my father who probably will not even look at the pictures I included here, much less read this thesis. I'm grateful for all the advice I received from you.

To my grandfather Iosif, who will probably be the only one in my family to read my work. I'm sorry I cannot follow in your footsteps, but I will strive every day to make you proud.

To Slava who patiently took care of all my computer-related problems. Thank you for all your help.

To Georgina, who first introduced me to Canada. Thank you! It was, quite literally, a life-changing experience.

To Jean and Denise who took me under their wing all those years ago. I cannot even begin to express what it meant for me.

To Sensei Saeki who taught me more about physics than some of my professors. Thank you for the wonderful opportunity you gave me when you let me join the Ottawa JKA family. The time I spent there was the best time of my life.

And last but not least, to Jean-Philippe. Meeting you was the best thing that ever happened to me.

Table of Contents

List of Tables

List of Figures

Chapter 1

Introduction: Amyloid β Protein in Alzheimer's Disease

Alzheimer's Disease (AD) is a chronic neurodegenerative disorder that is the most common form of dementia[1–9]. AD is mostly prevalent among the elderly population[6, 7, 9]. Reports show that 37 million people worldwide are affected by this disorder[7, 10]. Patients suffering from AD exhibit severe memory loss and mental degradation[2, 6, 8, 9, 11]. It has been shown that the clinical impairment in AD correlates with an early synaptic dysfunction[12].The dysfunction is then followed by more severe neuronal changes, including increased synaptic loss, widespread neuritic dystrophy, intracellular neurofibrillary tangles, extracellular neuritic (senile) plaques, and neuronal death[5–10, 12, 13]. Previous studies have shown that the general feature in the cellular pathology of AD is the disturbance of membrane-related events. The abnormalities in the cellular membrane structure and function include changes in brain phospholipid metabolism, disordering of cortical myelin and alterations in the molecular dynamics of hippocampal membranes[13].

The senile plaques, mentioned above, are believed to be one of the central hallmarks of the AD pathology[2, 5, 12, 14]. It is widely accepted that the major component of these plaques is the amyloid β-peptide (Aβ)[2–8, 10–19]. It has been shown that the sites in the brain of AD patients where neurodegeneration has occurred are associated with increased

Aβ deposits[15]. This observed correlation between AD pathology and Aβ presence has led to formation of the so-called "Aβ hypothesis", which states that formation of the toxic Aβ along with its excess deposition is the early step in the pathogenesis of AD that triggers its characteristic neurodegenerative changes[3, 5, 15].

The Aβ peptide is composed of 39-42 amino acid residues[1, 3, 4, 7, 8, 13, 14, 17, 18, 20]. An example of amino acid sequence for Aβ that has 42 residues is shown in Figure 1.1. Aβ originates naturally from cleavage of the larger transmembrane protein known as amyloid precursor protein (APP)[1–8, 11–16, 18, 20, 21]. Aβ is an amphiphilic peptide having a hydrophilic and a hydrophobic part. The hydrophilic part corresponds to the extracellular part of APP, while the hydrophobic part forms from APP's membrane-spanning domain[4, 5, 21]. There are two forms in which Aβ can exist: soluble and fibrillar[13]. The soluble form of Aβ is a part of normal product of APP cleavage. It is present in nanomolar concentrations in the cerebrospinal fluid and blood circulation under physiological conditions in healthy individuals and AD patients[12, 13, 22]. On the other hand, the insoluble Aβ fibrils are the main constituents found in the AD senile plaques[8, 13, 14]. In vitro studies have shown that formation of Aβ fibrils requires concentration of the soluble Aβ to be 4-5 orders of magnitude greater than the physiological concentration[14, 22, 23], although lower concetrations could be required for in vivo fibril formation[23]. It has been suggested that the conversion of soluble Aβ into its fibrillar form is a critical step in the onset of AD[15].

The soluble Aβ exists in α-helical form, while the insoluble Aβ is rich in β-sheet structures[3, 5, 8, 11, 14, 22, 24]. Formation of the β-sheets results from mis-folding of the α-helices. Unfortunately, causes for this mis-folding remain unknown[11]. The conversion process of the α-helical Aβ into fibrils involves formation of intermediate nonfibrillar oligomers. Current evidence suggests that these oligomers are even more toxic than the Aβ fibrils they mature into[1, 5, 8, 11, 14].

Figure 1.1 summarizes the above information regarding the origin of Aβ and its structural conversion from an α-helix to a β-sheet. The figure shows APP being cleaved by the enzymes β- and γ-secretases[1, 4, 5, 20, 25]. The β-secretase enzyme is responsible for production of the hydrophilic part of the Aβ protein, while the γ-secretase produces the hydrophobic part[1, 5]. The amyloidogenic processing of APP results in a normal soluble form of Aβ which then mis-folds into the β-sheets[26]. It has been shown that lipid raft sections of cell membrane tend to be the binding sites for Aβ and its subsequent aggregation into fibrils[2, 5, 10, 22, 27]. The current hypothesis is that the Aβ fibril formation is a nucleation-dependent polymerization mechanism in which the Aβ monomers assemble into micelles (as a sort of ordered nuclei)[1, 5, 13, 14, 21]. Once the concentrations reach a level that is above the critical micelle concentration the fibrils nucleate within the micelles. The lipids that constitute lipid rafts act as the seed that initiates this polymerization[1, 5].

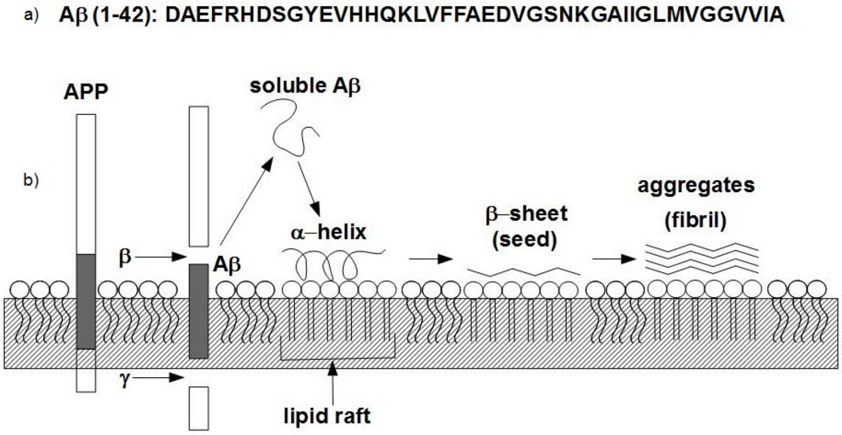

Figure 1.1: Formation and structural conversion of Aβ. Adapted from[5]. a) An example of Aβ peptide that has 42 residues. b) The cleavage of APP by β- and γ-secretase and subsequent production of soluble Aβ, which is later converted into insoluble β-sheet structure. Here for illustrative purposes the micelle formation is not shown. Instead the polymerization is shown taking place after one monomer acts as a seed.

The Aβ senile plaque formation is strongly associated with the cellular membrane of neurons[11]. The leading hypothesis for molecular basis of Aβ toxicity states that aggregated (fibrillar) Aβ interacts with the cell membrane and disassembles the lipid bilayer structure, thus altering the physiochemical properties of the neuronal membranes[4, 5, 21]. However, the majority of research up to now has been focused on investigating the behavior of Aβ in solution, therefore the exact mechanism of Aβ membrane interaction and toxicity is still unknown[1, 2, 4, 11, 21, 28]. Various studies conducted over the past several years point to several ways in which Aβ is affecting the membrane. The most prominent effect of Aβ appears to be the formation of ion channels[2–4, 11, 14, 17, 28]. These channels allow uncontrolled flow of ions, mostly Ca^{+2}, into the cell. This leads to excessive calcium influx and disrupts the normal cellular calcium homeostasis, leading to cell death[10, 12, 14, 17, 24]. Other effects of Aβ on the cellular membrane include increased fluidity[1, 10, 11, 28], induced thinning[11, 14, 16], reduced conductance[11, 12], and amyloid peptide channel formation (or activation)[4, 10]. Aβ may also be responsible for generation of reactive oxygen species (free radicals)[4, 5, 10, 22, 28]. Some of these effects are summarized in Figure 1.2.

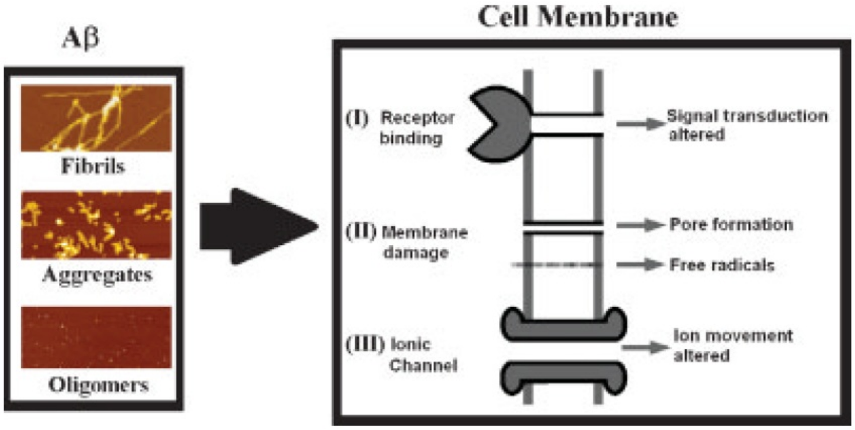

Figure 1.2: During conversion into its insoluble form, Aβ forms intermediate nonfibrillar oligomers, which then aggregate to form the Aβ fibrils implicated in AD. Aβ toxicity has been shown to manifest itself in various ways: I) altering signal transduction, II) causing pore and free radical formation, and III) ion-channel formation[10].

Despite all the recent efforts, the exact mechanism of Aβ toxicity towards a cell membrane is not well-understood[9]. The determination of this mechanism, however, is of utmost importance, since the membrane presents the first site of Aβ interaction with neurons, which in turn maybe be the origin of Aβ neurotoxicity. Knowing how Aβ behaves can be of great future benefit, since analogous amyloidogenic proteins have been implicated not only in AD, but also in Parkinson's disease, type 2 diabetes, and prion disease[14, 24, 27].

A good place to begin the study of Aβ-membrane behavior is to consider Aβ interaction with a well-defined model system that mimics the neuronal membrane[1, 2, 4].

In this work I present the results of a preliminary study of several lipid monolayers. The purpose of the study was to use atomic force microscopy imaging to find a lipid composition that can be used as a model of neuronal membrane for subsequent studies of Aβ interaction as related to AD.

In my research I was looking for a model membrane that would possess heterogeneous topography, i.e. exhibit structural domains, while incorporating the lipids most commonly found in neuronal membranes. The existence of domains was crucial, since we would like to later test a hypothesis that the membrane heterogeneity plays an important role in binding and fibrillization of Aβ. I was also looking for such a model that could illustrate if there is a difference in topography of a healthy membrane and a membrane affected by AD. The hypothesis being that a healthy membrane will have a smooth topography with smaller domains, which will get bigger and more prominent in a diseased membrane.

Chapter 2

Theoretical Background

Experimental studies of lipid membranes generally have three main components associated with them: membrane of choice, sample preparation and sample imaging or analysis[3, 4, 12, 21, 22, 28]. In this chapter I will outline the theoretical background behind these components as it pertains to my project. I will give an introduction to biological membranes, the theory behind Langmuir-Blodgett deposition technique, as well as the theory behind atomic force microscopy.

2.1 Introduction to Biological Membranes

The cellular (or biological) membrane is the "envelope" that surrounds every cell and, in the case of eukariotic cells, the organelles inside. The main functions of the membrane include defense against harmful species, molecular transport to and from the cell, chemical signaling to neighboring cells and interior organelles, cellular adhesion, and structure maintaining[29–33].

2.1.1 Phospholipid Bilayer

The membrane exists in a form of a bilayer - two layers of molecules. The molecules making up the bilayer are called lipids. The major class of membrane lipids is known as phospholipids[34]. They are a type of complex lipids that consist of a polar head group joined to a phosphate, which in turn is attached via a glycerol molecule to two hydrocarbon (fatty acid) chain tails[29, 32, 35]. The structure of a phospholipid is given in Figure 2.1. The head group of a phospholipid is polar, hence hydrophilic, while the two tails are nonpolar, hence hydrophobic. Therefore phospholipids are classified as amphiphilic molecules, i.e. molecules possessing both hydrophilic and hydrophobic parts.

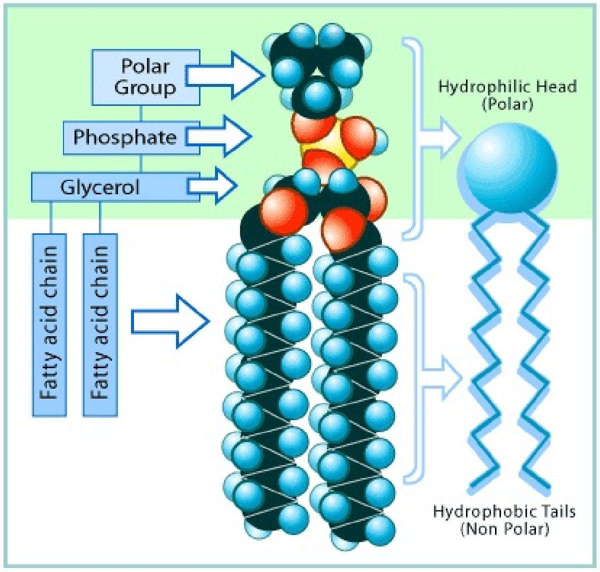

Figure 2.1: A space-filling and schematic diagram of a phospholipid[36]. The hydrocarbon tails are attached to the phosphate headgroup.

When in a solution, such as the physiological conditions for cells and organelles, phospholipids spontaneously form the bilayer membrane in the process know as hydrophobicity-driven self-assembly[24, 29]. Due to their amphiphilic nature the molecules have a specific orientation in the bilayer - the hydrophobic tails are pointing inward and the hydrophilic heads outward facing the extracellular fluid. This orientation is shown in Figure 2.2.

A useful concept for visualizing some of the characteristics of the bilayer is its lateral pressure profile, an example of which is given in Figure 2.3. Such a profile illustrates the forces parallel to the plane of the lipid membrane as a function of distance from the centre of the bilayer[24]. There are three forces shown in the profile (Figure 2.3): (i) a steric repulsion between the lipid headgroups, (ii) entropic repulsion due to thermal motion of the phospholipid tails inside the bilayer, (iii) the cohesive force arising from the interfacial tension due to the hydrophobic effect[24]. Naturally, when the system is stable (in equilibrium), the net force acting on it is zero. This is achieved by having the interfacial tension balanced by the combination of the headgroup and chain repulsion. Therefore, at equilibrium the membrane is tension free. The packing density of the lipids then correspond to an equilibrium lateral pressure, a value of 30-35 mN/m for biological membranes[24, 28, 37, 38].

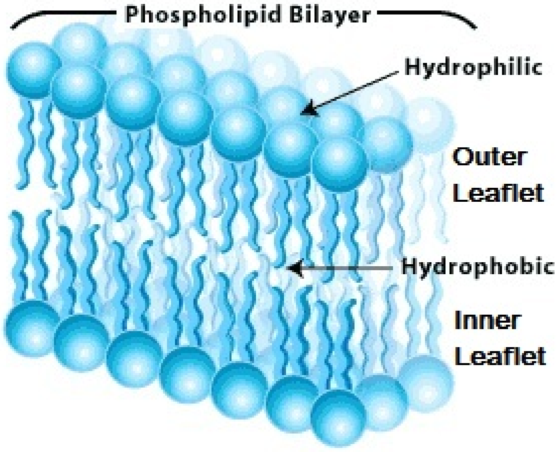

Figure 2.2: The assembled phospholipid bilayer with the tails on the inside and heads on the outside[39]. The entire bilayer acts as a two-dimensional liquid[40].

There are many different phospholipids that can make up the bilayer membrane. They are defined by the nature of the polar group attached to the phosphate. For example, phosphatidylcholine has a choline head group, and phosphatidyllethanolamine has an ethanolamine head group. The head group nature affects the interactions between the membrane and other molecules[35]. The degree of saturation of the hydrocarbon chains of the tails can also vary between different phospholipids. For example, dipalmitoylphosphocholine (DPPC) has no double bonds on the two hydrocarbon tails[41] and dioleoylphosphocholine (DOPC) has a double bond on each of its hydrocarbon chains[42]. The degree of saturation determines if the tails are “straight” (no double bonds) or “bent” (some double bonds) which has a direct effect on the fluidity and packing density of the membrane[35]. It is important to note that, since there is a wide variety of phospholipids, the composition of the inner and outer leaflet of the membrane is not necessarily the same[35].

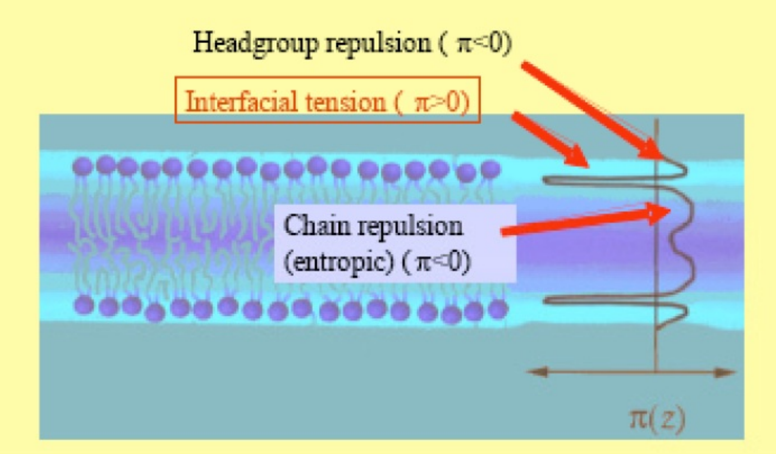

Figure 2.3: An example of a lateral pressure profile for a phospholipid bilayer[24]. The graph illustrates the forces that are parallel to the plane of the lipid membrane as a function of distance from the bilayer center.

2.1.2 Fluid Mosaic Model and Lipid Rafts

The Fluid mosaic model is the current model for the membrane structure. It was proposed by Singer and Nicolson in 1972[7, 10, 30, 32]. In this model the membrane is treated as a two-dimensional liquid formed by the phospholipid bilayer with globular proteins floating in it. The proteins that span the entire membrane and in some cases project on one or both sides of it are known as integral proteins. The proteins that are attached to one side of the bilayer are known as peripheral proteins[30, 32]. The model is illustrated in Figure 2.4.

The integral proteins form channels for passage of specific molecules under specific conditions. They also form receptors whose function is to sense exterior conditions and ion pumps that pull certain ions across the membrane. The peripheral proteins communicate information from the receptors to the interior of the cell[29, 32, 33].

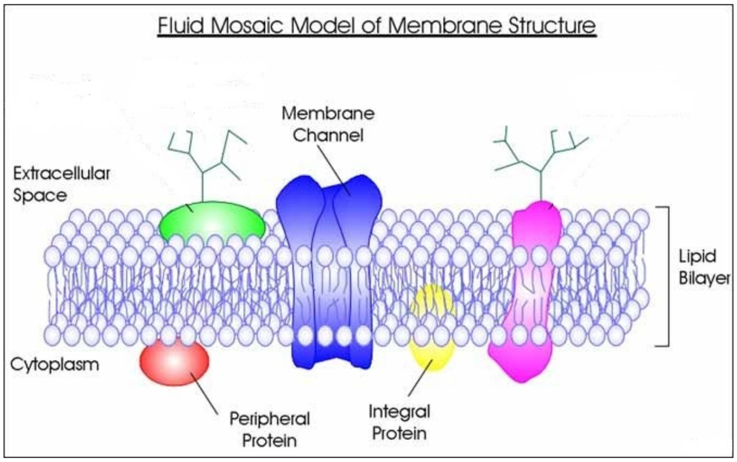

Figure 2.4: A graphical representation of the fluid mosaic model of cell membranes. Adapted from [43].

The fluid mosaic model, although still preferred by most scientist, does not allocate any functional significance to physical heterogeneities in the lipid organization[31]. These heterogeneities result from both lipid-lipid and lipid-protein interactions and tend to manifest dynamic fluctuations on different time scales (i.e. both long and short term heterogeneities are possible)[24]. In 1997, Simon and Ikonen proposed the "lipid raft" hypothesis that can complement the fluid mosaic model[38, 44, 45]. Lipid rafts are structural dynamic microdomains in the membrane that are enriched in cholesterol and glycosphingolipids (especially sphingomyelin)[2, 6, 7, 10, 27, 37, 38, 40, 45–50]. The rafts are characterized by tight packing of lipid acyl chains but high mobility of the individual lipids[37, 51]. The ordered phases a bilayer can exhibit are classified by conformational degrees of freedom of the hydrocarbon chains. In the absence of cholesterol, the bilayer may exist in two phases: the gel at low temperature and the liquid disordered (L_d) state at high temperature[10]. The latter is the state that is found in physiological conditions[10, 31]. Increasing amounts of cholesterol cause the formation of a third state: liquid-ordered (L_o), which can be thought of as an intermediate state between the L_d phase and the gel phase[10]. This new phase effectively creates the so-called raft surrounded by the bulk of the liquid disordered state[7, 10, 27, 37, 52]. This is shown in Figure 2.5. The formation of the L_o due to the presence of cholesterol can be explained by cholesterol's flat and rigid molecular structure[40, 51], as shown in Figure 3.1. This structure is able to impose conformational ordering on tail chains of a neighboring phospholipid, without causing a corresponding reduction of the translational mobility of the lipid[7, 10, 24, 40].

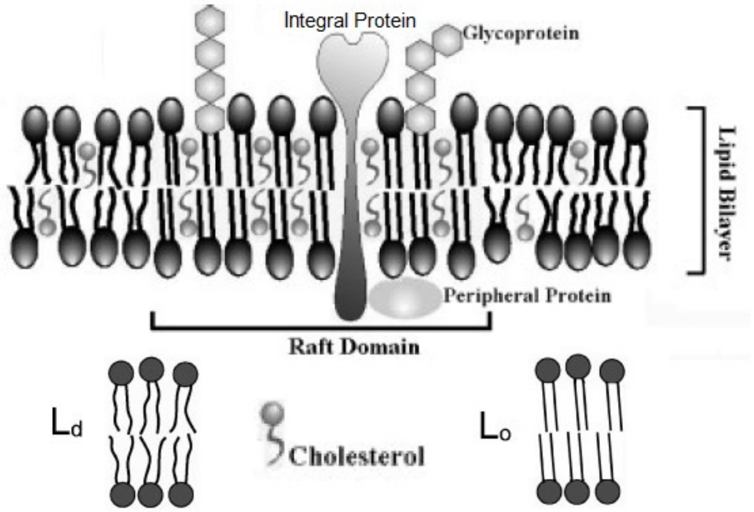

Figure 2.5: Diagram of the lipid raft model. Adapted form [10]. The presence of cholesterol induces the transition from the liquid disordered (L_d) to the liquid-ordered (L_o) phase. Sphingomyelin is not shown here, although it is usually also present in lipid rafts.

Lipid rafts are still an area of active study[40, 50, 53–57], since they have been implicated in a number of important membrane functions. Theses function include: signal transduction[2, 21, 27, 31, 44, 52, 58, 59], sorting of proteins and other membrane components[21, 31, 44, 52, 59], protein trafficking[2, 21, 27, 52], membrane fusion[58], and virus release[31, 58]. It was also shown that lipid rafts are the binding and transport sites for several pathogens and toxins, such as HIV-1[8, 27, 31, 52, 59]. In addition, as was mentioned in Chapter 1, lipid rafts appear to play a role in the toxicity mechanism of the Aβ protein[2, 5, 10, 22, 27] and, as such, are important to the research of the pathogenesis of Alzheimer's disease.

2.1.3 Membrane Composition

The overall composition of the membrane has three components: lipids, proteins and carbohydrates. On average, lipids are the most prominent one, constituting approximately 50% of the membrane[60]. The second largest component is proteins (45%), leaving 5% for carbohydrates[60–62]. In a eukaryotic membrane (eg. rat[61], mice[49], human[63]) there are three principal types of lipids: phospholipids (eg. DPPC, POPC, etc.), sterols (eg. cholesterol) and sphingolipids (eg. sphingomyelin)[60]. Phospholipids have the highest relative molar concentration: 40-60%[10, 60]. Sterols, mainly cholesterol, are a close second with a concentration of 30-40%, which leaves sphingolipids with 10-20%[10, 60]. An average eukariotic cell can be expected to contain on the order of tens of thousands of different phospholipids, with different types of cell and cellular organelles having their own specific composition. These compositions are highly dynamic and tend to adapt on different time scales to both physiological and pathological changes happening in the organism[24].

The cell type that is most relevant to my research project and to subsequent studies related to Alzheimer's disease is the neuron. However, the exact composition of neuronal cell membrane remains undetermined, largely because neurons are also divided into a diverse array of classes and types[61, 63, 64]. The available information shows that in general the neuronal membrane at least contains phosphatidylcholine (PC), phosphatidylethanolamine (PE), cholesterol, sphingomyelin, gangliosides, and different proteins in various proportions[6, 8, 49, 60, 61, 63].

2.1.4 Model Membrane

Since cellular membranes are not only structurally complex, but also differ from each other in several aspects that relate to their composition, it is very common to use models to study them[14]. These model membranes are artificially created to be structurally and compositionally simpler than real ones. The distinct advantage of model membranes is that they allow for systematic manipulation of the chemical composition and monitor the effects on structure, fluidity, etc[14]. Naturally, the models lack the complexity of biological membranes, since they don't usually incorporate integral membrane proteins and polysaccharides, althought it is possible to do so[65]. This leads to the main disadvantage of using models: the impossibility of discovering the complete picture of the biochemical processes (for example, of Aβ interaction with the membrane). However, the model membranes are very useful tools in providing a platform for hypotheses that can later be tested in more rigorous biological settings[14].

The model membrane systems are generally unilamellar vesicles (small, large or giant), monolayers or bilayers[10, 14, 40, 46, 52, 66]. In the context of my project, I am mostly concerned with the lipid monolayers as models for cellular membrane of neurons. A model lipid monolayer is a single row (layer) of molecules. A model monolayer has the advantages of being simple and quick to prepare and manipulate. There are two common methods of preparing synthetic monolayers (or bilayers, for that matter). The first method is to create them in solution in form of vesicles which are then adsorbed onto a substrate for imaging. The second method is called Langmuir-Blodgett deposition in which a substrate is dipped into a monolayer (or bilayer) formed at the air-water interface. This method is discussed in the following section. Lipid monolayers that have been adsorbed to a substrate are referred to as supported monolayers[35].

2.2 Langmuir-Blodgett Deposition Technique

The Langmuir-Blodgett (LB) technique is among a number of methods used to deposit an organic thin film (monolayer) on a solid substrate[67, 68]. It offers precise control of the film thickness, homogeneous deposition over large areas, the possibility of creating multilayer structures (e.g. bilayers) with varying layer composition, and, finally, the ability of deposition on almost any solid substrate available[67].

2.2.1 Langmuir Films

The term Langmuir film is used to describe a floating monolayer composed of surfactants trapped between two phases (usually liquid and gas)[67, 68]. A surfactant is a surface active agent that can reduce the surface tension at the interface between the two phases[40, 69].

The easiest way of demonstrating the surface chemistry behind Langmuir films is to consider a water-air (liquid-gas) interface. The water molecules possess a certain degree of attraction to each other (cohesion). In the bulk of water these interactions are balanced by equal attractive forces in all directions. The molecules at the water surface (i.e. the air-water interface), however, experience an imbalance: larger attraction towards the liquid phase than the gas phase. This leads to a net attractive force in the direction of the bulk of water, causing the air-water interface to minimize its area (contract). This is illustrated in Figure 2.6. The net effect of the situation is the presence of free energy at the water surface. The presence of this surface free energy (in J/m^2) is essentially equivalent to water surface having a line (or surface) tension (in N/m). Thus, surface tension can be described as a measure of cohesive energy present at the interface[67].

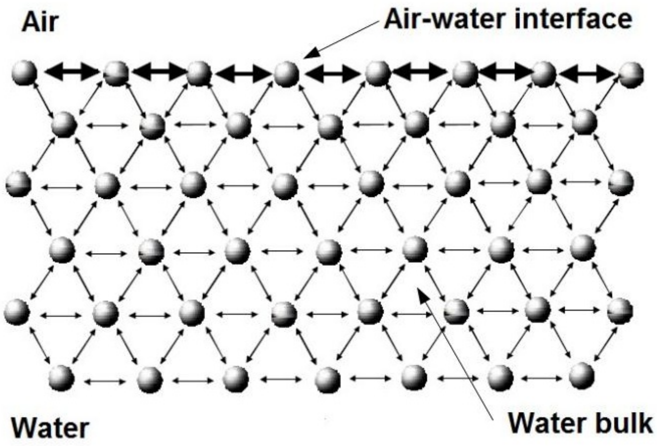

Figure 2.6: A schematic illustration of the molecular interaction at the air-water interface and in water bulk. It is clear that the attractive forces felt by the water molecules are balanced in the bulk but not at the interface, causing the presence of free energy at the water surface. Adapted from [67].

As was mentioned earlier, surfactants are capable of reducing the surface tension at the interface by lowering the intermolecular attraction at the surface and increasing the entropy[67]. Surfactants are amphiphilic molecules (e.g. phospholipids) - they have a hydrophobic tail group and a hydrophilic head group. A surfactant can be deposited at an air-water interface by first dissolving it in non-aqueous volatile solvent. Once deposited on the water surface, the solvent evaporates, leaving the surfactant behind[67–69]. Surfactant's amphiphilic nature is responsible for its orientation at the air-water interface: polar hydrophilic head group is pulled into the water bulk and the nonpolar hydrophobic tail (or tails) points up in the air[67, 68]. Sweeping a barrier over the water surface causes the surfactant molecules to compress into an ordered monolayer, forming a Langmuir film[68]. This is shown in Figure 2.7.

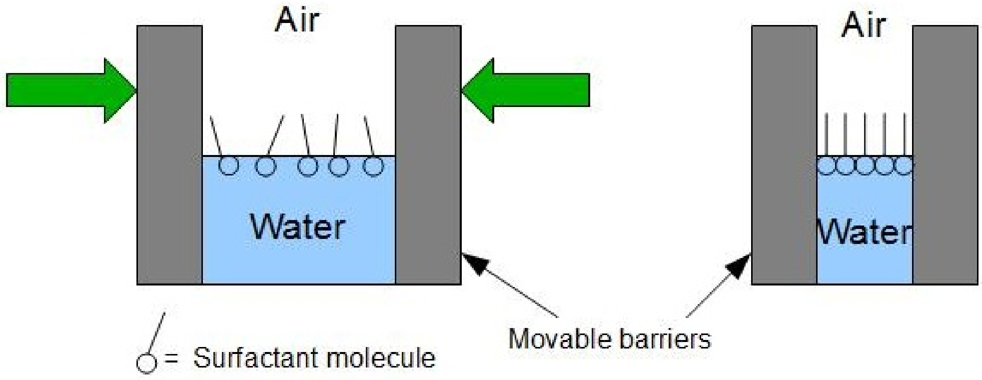

Figure 2.7: A diagram showing the orientation of the surfactant molecules at the air-water interface: the hydrophilic head is in the water and the hydrophobic tail is in the air. Reducing the surface area available to the molecules using a movable barrier results in formation of a compressed floating monolayer known as Langmuir film.

When surfactant is deposited on the water surface it spreads out to cover all the available area. If this area is large the distance between adjacent molecules is also large, which means that their interactions between themselves are weak. In this case the monolayer behaves as a two-dimensional gas and has little effect on the surface tension of water. However, when the available area is reduced using the barriers, the surfactant molecules begin to have a repulsive effect on each other. This effect is a two-dimensional analogue of pressure known as surface pressure, Π. The expression for surface pressure is given by Equation 2.1[32, 67–69],

$$\Pi = \gamma_o - \gamma \tag{2.1}$$

where γ_o is the surface tension without the surfactant and γ is the surface tension with the surfactant present.

2.2.2 Langmuir-Blodgett Trough

The Langmuir-Blodgett (LB) trough, also known as the LB surface balance[32, 67], consists of a trough, a movable barrier (or barriers) and a pressure sensor. A schematic diagram of a generic LB trough is given in Figure 2.8. The trough usually contains an aqueous subphase (water-based or pure water), onto which the surfactant is deposited to form a monolayer. The surface area of the trough can be varied using the movable barriers.

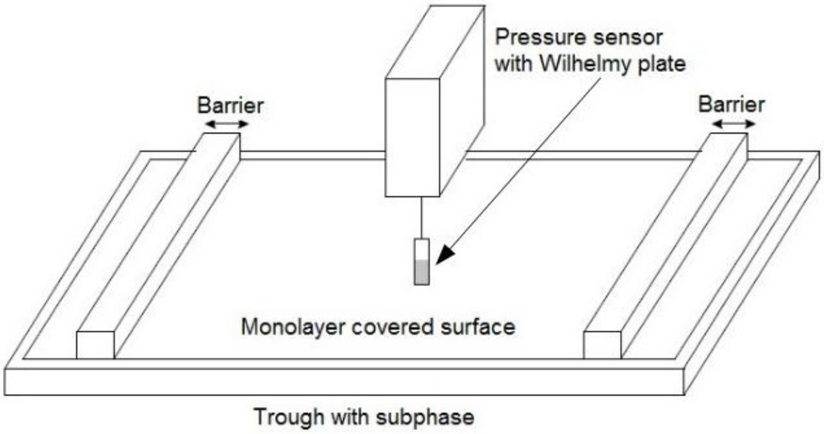

Figure 2.8: A schematic diagram of a generic Langmuir-Blodgett trough. The subphase with the surfactant monolayer is contained in a trough. The movable barriers allow for control of surface area covered by the monolayer. The pressure sensor uses a Wilhelmy plate to monitor the surface pressure (reduction in surface tension[68]). Adapted from [67].

The surface pressure of the monolayer is monitored using the pressure sensor equipped with a Wilhelmy plate. The measurement of the pressure is obtained by determining the force due to surface tension on a plate suspended above and partially immersed in the subphase. The force is then converted into surface tension using the dimensions of the plate[67, 68]. The plate can be made of a variety of material, such as chromatography paper, glass, quartz, platinum, or mica[67, 68]. Figure 2.9 shows the dimensions (width w, length l, thickness t) of a plate partially immersed to a depth h.

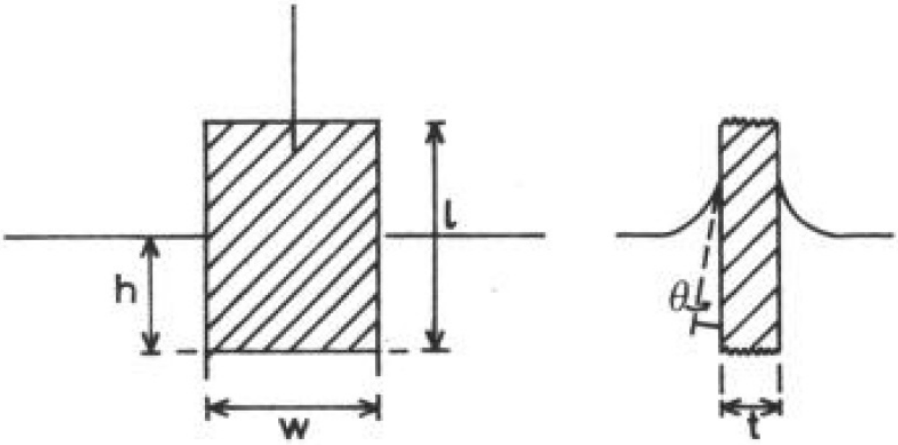

Figure 2.9: The Wilhelmy plate partially immersed in the subphase[67]. The plate has width w, length l, thickness t and is immersed in water to a depth h. The angle θ represents the liquid-to-plate contact angle.

The forces acting on the plate consist of gravity, upthrust (buoyancy) and surface tension (downward)[67, 68]. Let ρ_p be the density of the plate material and ρ_L - the density of the liquid subphase. Let θ be the contact angle of liquid to plate, as shown in Figure 2.9. Then the expression for net force on the plate in the downward direction is[67, 68]:

$$F = (\rho_p lwt)g + 2\gamma_L(t + w)cos\theta - (\rho_L twh) \tag{2.2}$$

where g is the acceleration due to gravity and γ_L is the surface tension of the liquid. The first term in Equation 2.2 represents the gravitational pull on the plate, the second term is the downward acting surface tension and the third term is the upthrust that pushes the plate up. The pressure is usually zeroed prior to start of any experiment, thereby eliminating the gravity term. The upthrust is eliminated by keeping the plate at constant level by the pressure sensor, regardless of the value of the surface tension. When paper plates (e.g. chromatography paper) are used, they become completely wetted after some time, resulting in the contact angle of 0^o[67, 68]. Therefore, Equation 2.2 reduces to:

$$F = 2\gamma_L(t + w) \tag{2.3}$$

Preforming a very simple rearrangement of Equation 2.3 gives the expression for surface tension:

$$\gamma_L = F/2(t + w) \tag{2.4}$$

As was mentioned in the previous section, the surface pressure is equal to the change in surface tension that results from addition of a surfactant (Equation 2.1.). Therefore, the value of the surface pressure is obtained from the change in γ_L once the surfactant is introduced onto the subphase.

Surface pressure monitoring is very important during a deposition process. The LB trough can be used to create highly organized multilayers of the surfactant. This is accomplished by successive dipping of a solid substrate up and down through the Langmuir film (floating monolayer) while simultaneously keeping the surface pressure constant through a computer controlled feedback loop[67, 68]. During this process the floating monolayer is adsorbed to the solid substrate forming a structure known as Langmuir-Blodgett film. Depending on the number of times the substrate is dipped into the subphase, the produced LB films can be as many as hundreds of layers thick[67].

The solid substrate used for deposition can be hydrophobic or hydrophilic. For a hydrophobic substrate the first layer is deposited by lowering it into the subphase through the monolayer, such that the tails of the surfactant will adhere to the substrate (refer to Figure 2.7 for surfactant orientation at the interface). In the case of a hydrophilic substrate, the first layer is deposited by raising it from the subphase through the monolayer, such that the surfactant heads adsorb on it, leaving the tails pointing in the air. For the purposes of my project, it is the latter case that I'm concerned with: the deposition of a single layer of surfactant onto a hydrophilic substrate (mica). The process is shown in Figure 2.10: first the substrate is lowered into the subphase, then the surfactant is introduced, then the substrate is raised through the surfactant monolayer.

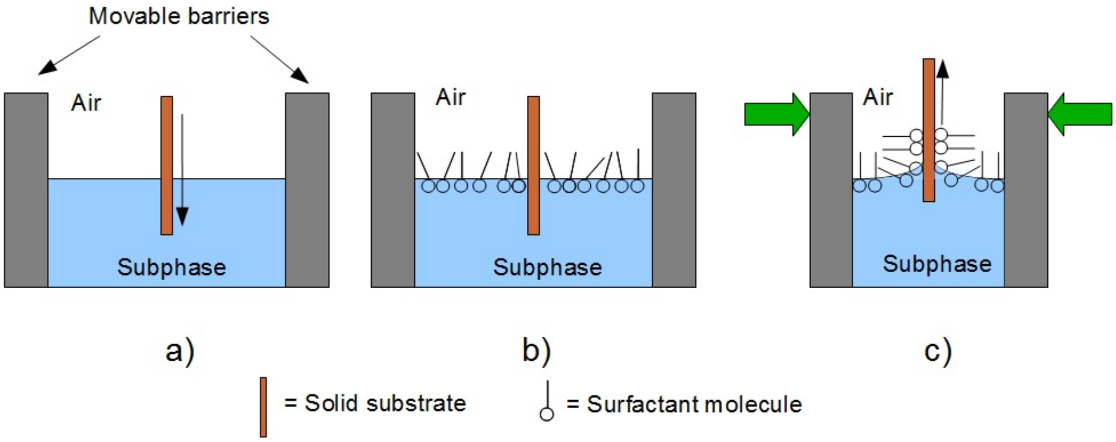

Figure 2.10: Schematic diagram of deposition of surfactant molecules onto a hydrophilic solid substrate (such as mica) to form a monolayer. a) First, the substrate is lowered into the subphase. b) The surfactant molecules are then introduced onto the subphase. c) The movable barriers are used to maintain a constant deposition surface pressure. The substrate is slowly raised out of the subphase. As the substrate passes through the monolayer, the heads of surfactant molecules adsorb onto it leaving tails pointing into the air. A thin layer of water (not shown here) usually remains trapped between the hydrophilic substrate and the headgroup.

2.2.3 Pressure-Area Isotherms

Aside from monolayer deposition, the LB trough can be used to study monolayer characteristics on a subphase surface using a pressure-area isotherm (where "pressure" refers to surface pressure, as defined in Equation 2.1). This isotherm shows the changes in surface tension that take place during a monolayer compression[68]. As was already mentioned in the previous section, the change in the surface tension is equivalent to the surface pressure.

A pressure-area isotherm is collected at constant temperature (hence, the name "isotherm") by compressing the surfactant monolayer film using the movable barriers at a constant rate, while continuously monitoring the surface pressure by means of the Wilhelmy plate balance[67–69]. The shape of the isotherm is a unique characteristic of the surfactant molecules[32, 68, 69]. A schematic pressure-area isotherm is shown in Figure 2.11. The distinct regions on the isotherm are the phases that the monolayer exhibits during compression. The exact phase behaviour of a given surfactant depends on its physical and chemical properties, as well as, subphase temperature and composition[67].

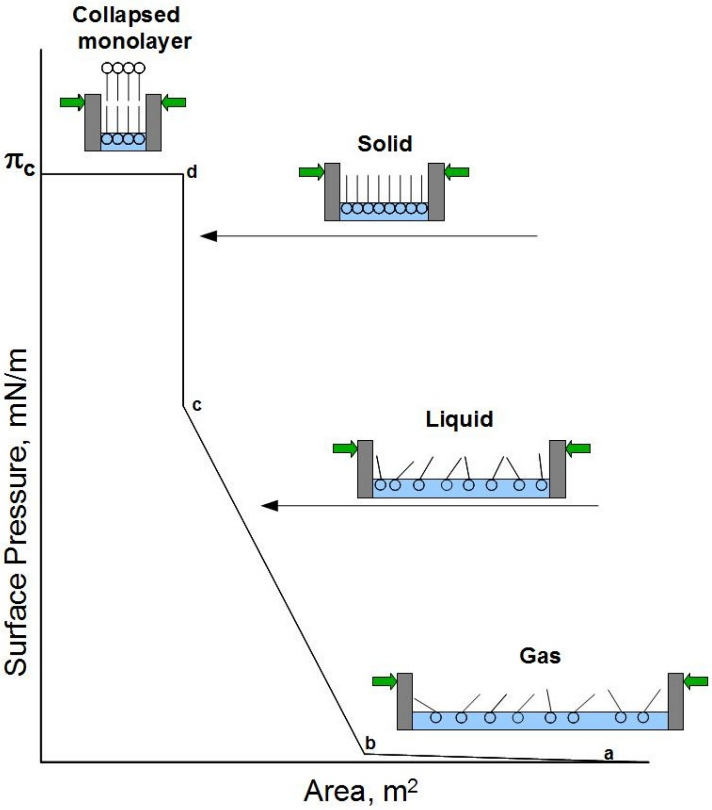

Figure 2.11: A schematic diagram of a pressure-area isotherm. The distinct regions represent the phases that the surfactant monolayer exhibits during compression: Gas: a-b, Liquid: b-c, Solid: c-d. The orientation of monolayer molecules is shown for each corresponding phase. The highest pressure to which the monolayer can be compressed before it collapses is designated as π_c. Adapted form [66–68].

On average, the pressure-area isotherms of various surfactants consist of three distinct regions: gas, liquid and solid region (see Figure 2.11). After the initial spreading of surfactant onto the subphase, before any compression was done, no external pressure is applied to the monolayers. Therefore, the molecules behave as a two-dimensional ideal gas[68, 69]. During compression some ordering is imposed on the molecules causing them to undergo a phase transition from gas to liquid (two-dimensional). Continued compression increases the density of the monolayer until it reaches the solid phase. If the monolayer is further compressed after reaching the solid phase, it will collapse into a three dimensional structure. The collapse occurs when the exerted force (from the compression barriers) becomes too great causing molecules to be ejected from the plane of the monolayer into either the subphase or the air[68]. The highest pressure to which a monolayer can be compressed without a detectable movement of the molecules in the Langmuir film to form a new phase is known as the collapse pressure, π_c [32, 66–69]. The magnitude of the π_c is related to the nature of the surfactant and it's interaction with the subphase[66].

2.3 Atomic Force Microscopy

The samples prepared using LB deposition technique can be studied using various methods. The method that I used in my project is atomic force microscopy. Since learning how to operate such a microscope was by far the biggest challenge I had faced, I will elaborate on its operational principles in great detail.

Atomic force microscope (AFM) is an imaging technique which is able to achieve nanoscale (atomic) resolution of surface structures of various samples[70]. The AFM was invented in 1986 by Binning, Quate and Gerber[71–73]. In the original paper, Binnig et al. (1986) presented AFM as a combination of the scanning tunneling microscope (STM) and the stylus profilometer that can be used to study conductors and insulators on an atomic scale. The principle of AFM operation, as explained by Binnig et al. (1986) is shown in Figure 2.12. A cantilever with a sharp tip at the end is at the heart of the AFM. It moves over the sample surface in a raster (line-by-line) scan pattern and bends in response to the force of interaction between the tip and the surface. This vertical bending of the cantilever is then translated into information about the sample topography[72, 74]. Since 1986 AFM has evolved into a highly versatile and very popular scientific tool. Some of the characteristics of modern AFMs include high force sensitivity (ability to measure forces in the pico-Newton range[70, 74]), high positioning accuracy (on the order of 0.01nm[70]) and the ability to provide 3D images of unprecedented resolution[74, 75].

AFM can be used to investigate virtually any sample surface (insulating, non-conducting or conducting[70]) of interest[76]. One of the main benefits of AFM that makes it a very popular tool for various biological studies is that the sample does not require extensive preparations - there is no need for sample dehydration, embedding, metal coating, etc[77]. Another attraction of AFM is that samples can be studied under their physiological conditions[70]: in air, in liquid or gas environments over a wide range of temperatures[78, 79].

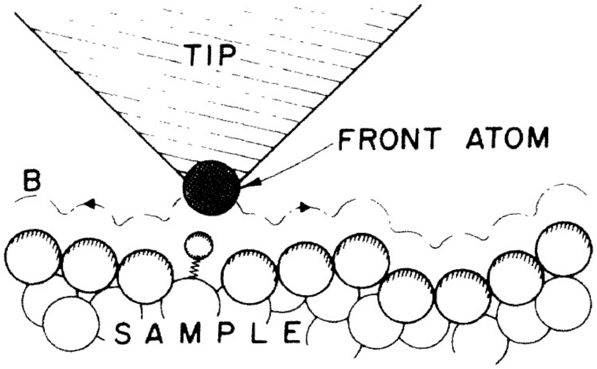

Figure 2.12: The adapted illustration of the basic principle of operation of an AFM as was presented by Binnig et al. (1986) in their original paper. The sharp tip is moved along the contour B in such a way as to maintain a constant force of interaction between the tip and the sample[71].

As was already mentioned above, in an AFM the probing tip is attached to a cantilever. The attractive and repulsive forces between the tip and sample surface cause the cantilever to bend (deflect away or towards the surface), as shown in Figure 2.13. The images are created by scanning either the tip or the surface[35] in an x- and y-direction. The deflection of the cantilever (observed with a detector) as a function of the lateral (x,y) position is then digitized to produce the image[80]. The sample itself is mounted on a scanner that regulates it's 3D positioning with high precision[74]. A feedback system is used to monitor the cantilever response and make the necessary adjustments depending on the imaging mode[81]. This basic outline of the principle of operation of an AFM is schematically illustrated in Figure 2.14a. It is clear that the main components of an AFM setup are the scanner, the detector, the cantilever, and the tip[73, 74]. The sample holders are important depending on the type of imaging environment required: air/gas or liquid. The function and properties of these components, as well as, operation modes of an AFM will be elaborated on in the following sections.

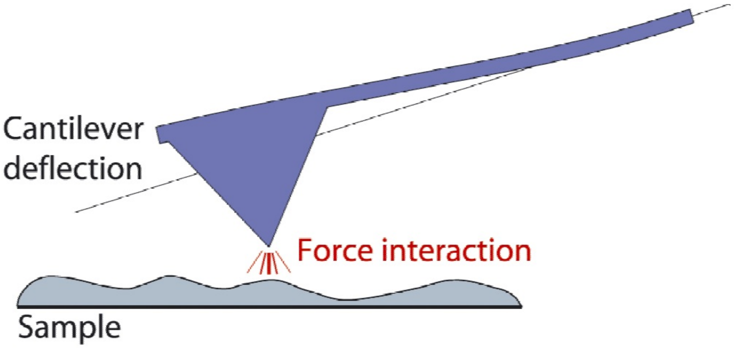

Figure 2.13: The interaction forces between the tip and the sample surface cause the cantilever deflection. This deflection is measured and used to form a 3D image of the sample[81].

The actual AFM setup is fairly compact. It requires a connection to an electronic controller, a computer and two screens (usually). The latter enables simultaneous monitoring of sample image and experimental parameters[82]. An example of such a setup is shown in Figure 2.14b.

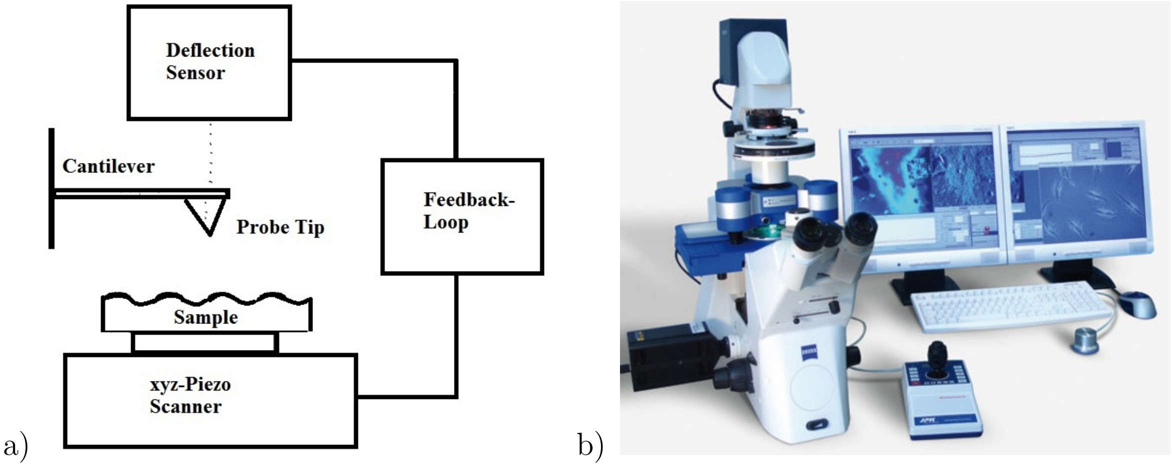

Figure 2.14: The AFM setup. a) Schematic representation of the basic principle operation of an AFM. The probe tip is mounted on the cantilever. The sample is mounted on the piezo scanner. The deflection sensor (detector) monitors cantilever deflections caused by the tip-sample interaction force. The feedback loop can be used to keep the deflection constant if necessary[80]. b) An example of an AFM setup. The electronic controller is not shown. The AFM depicted in this picture is a JPK instruments NanoWizard AFM that has an inverted optical microscope integrated into the setup[83].

2.3.1 AFM Components: Scanner

The sample position in an AFM is controlled by the piezoelectric scanner that moves the sample in three dimensions (x,y,z) with respect to the cantilever. Alternatively, in some AFMs it is the cantilever, instead of the sample, that is mounted on the scanner[35, 73]. In both cases, the scanner is made from piezoelectric material. As the name suggests, this material relies on piezoelectric effect - generation of a potential difference across the opposite faces of certain ceramics or crystals as a result of applied mechanical stress. In an AFM, a potential difference is applied to the scanner material that results in its elongation or contraction (depending on the voltage polarity)[35, 84]. This effect is shown in Figure 2.15.

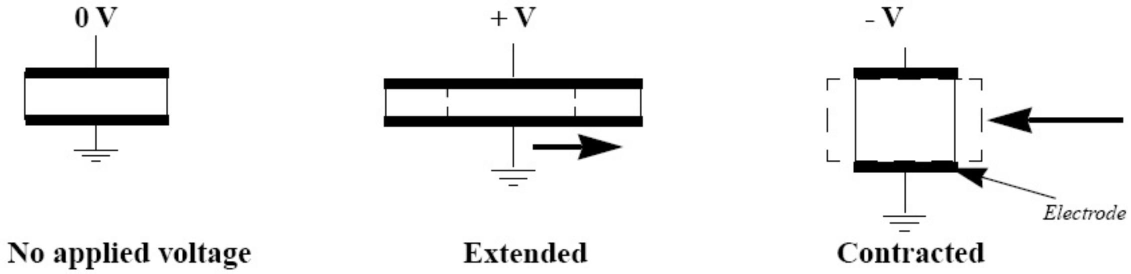

Figure 2.15: The effect of applied voltage on piezoelectric material[84].

Modern AFMs use so-called piezo tubes that are constructed by combining independently operated piezo electrodes for each of the 3 dimensions[84], as shown in Figure 2.16a. The tube is moved in the z-direction by applying a voltage between the inner and all the outer electrodes to induce contraction or elongation. Applying a voltage to just one of the outer electrodes induces bending of the tube, i.e. the movement in the x- and y-direction. It is this motion in (x,y) that produces the raster scan pattern (Figure 2.16b).

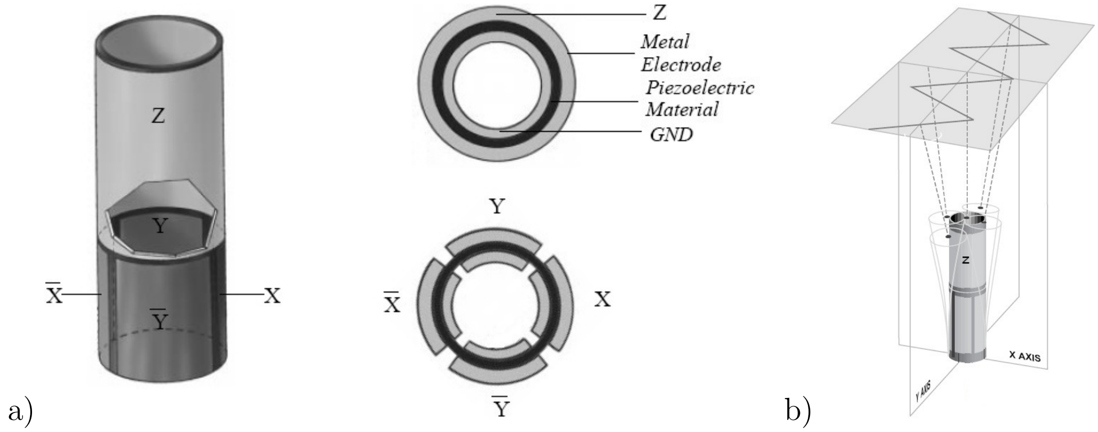

Figure 2.16: a) Schematic representation of a piezo tube scanner with the x-y-z configurations. b) Piezo movement during a raster scan. The scan pattern is produced due to application of voltage to the x- and y-axes[84].

2.3.2 AFM Components: Detector

As was already mentioned, the first detection technique used by Binnig et al (1986) was based on electron tunneling[71, 80]. Since then a number of other detection methods have been developed[35, 80]. The optical beam deflection (OBD) is the detection method that is most commonly used in modern AFMs[73, 78, 84–86]. In the OBD a light from a laser source is reflected off the back of the cantilever and is directed into a position sensitive detector (PSD). The PSD is usually a photodiode - a semiconductor device which turns light incident on it into an electrical signal (the brighter the incident light - the higher the electrical current)[35]. Changes in the laser beam reflection angle result from the cantilever deflection and cause the beam to fall on different parts of the photodiode. The principle of OBD is shown in Figure 2.17a.

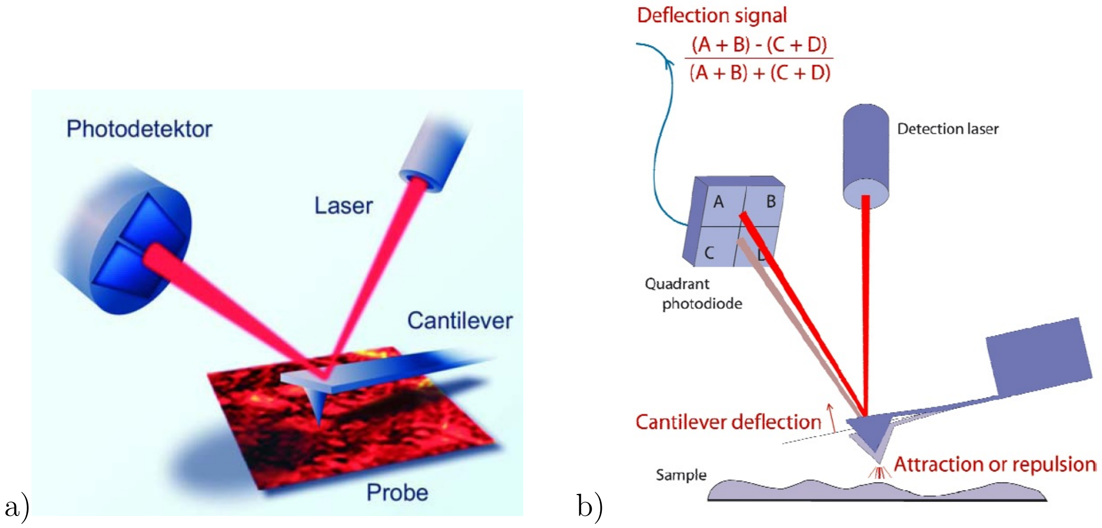

Figure 2.17: Optical Beam Deflection (OBD) Detector. The laser beam is reflected from the back of the cantilever and onto a photodector. a) Graphical representation of OBD. b) Schematic representation of OBD[81].

The photodiode is sometimes made of two quadrants, but most of the current AFMs have a four-quadrant photodiode[81] (Figur 2.17b). The deflection signal equation in Figure 2.17b represents the direct measurement of the vertical deflection of the cantilever: the difference between “top” (A+B) and“bottom” (C+D) intensities divided by the total intensity (A+B+C+D)[80, 81]. The vertical deflection is the measure of the interaction force between the tip and the sample surface. The lateral deflection (twisting) of the cantilever represents the frictional force acting on the tip and can be calculated in a similar manner by comparing the “right” (B+D) and “left” (A+C) sides of the photodiode[81].

2.3.3 AFM Components: Cantilever and Tip

AFM cantilevers are usually made from silicon (Si) or silicon nitride (Si_3Ni_4), with aluminum or gold coating at the back for added reflectivity.

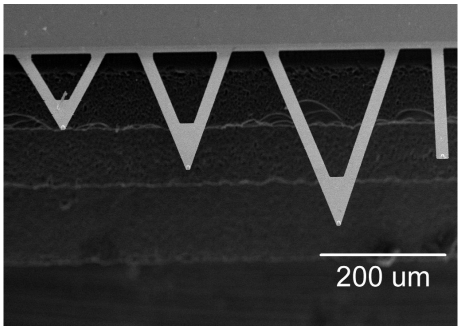

Figure 2.18: Scanning electron microscope image of AFM cantilevers. Two types of cantilever geometry (beam and V-shape) are clearly seen[87].

Cantilever dimensions range from 50 to 500 μm in length, 0.5 to 5 μm in thickness and 10 to 50 μm in width[75, 78, 81, 82]. Figure 2.18 shows an example of cantilever sizes and geometries.

The behavior of the cantilever is usually modeled as a spring that obeys Hooke's law[35, 70, 79, 81]:

$$F = -kx \tag{2.5}$$

where F is the force acting on the cantilever tip, k is the spring constant and x is the deflection of the cantilever. The negative sign indicates that force and deflection are acting in opposite directions. Currently, there is a wide variety of cantilevers available with spring constants ranging between 0.005 and 100N/m[81, 82, 84]. Some applications, such as biological imaging, call for soft (low-k) cantilevers, while others require stiffer (high-k) ones.

The tip is attached to the end of the cantilever (Figure 2.19) , but since it is only a few (~3 μm) microns long and often less than 10nm in diameter[75], it cannot be seen without a microscope. The tip is usually made of the same material as the cantilever.

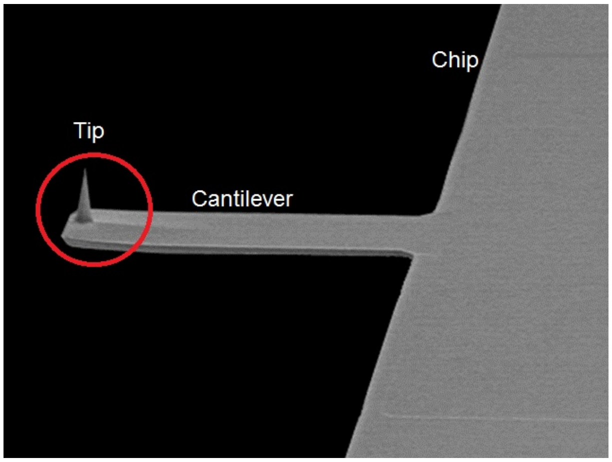

Figure 2.19: The AFM tip. The cantilever is mounted on a chip (of the same material). The tip is located at the cantilever end. Adapted from [88].

The shape of the tip can have a significant effect on the acquired imaged. This is illustrated in Figure 2.20. It is important to note that the image will always be a convolution between the sample surface topography and tip geometry[35, 81]. The tip might also become contaminated or chipped over time, which will also affect the resultant image.

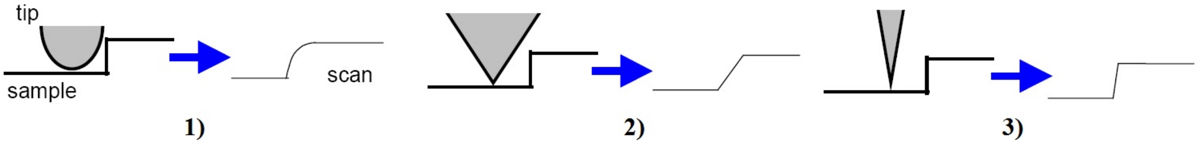

Figure 2.20: The effect of the tip shape on the resultant image. Note that none of the tips produce the exact image of the rectangular step on the sample surface[81].

2.3.4 AFM Components: Sample Holders

The little sample preparation that is required for an AFM study involves, among other things, mounting the sample to be imaged. When imaging in air, some samples can be simply attached to a small metal disk with double sided conducting adhesive tape[35]. However, in biological applications of AFM the samples cannot be simply taped to the base of the microscope. In imaging biological samples it is customary to deposit them onto a solid substrate or use liquid cells (when imaging in liquid is required).

There are a few requirements that the substrate has to meet to be “eligible” for sample deposition. It must have an appropriate affinity for the sample - allowing adsorption, but keeping the sample partially functional at the surface[86]. The substrate should be relatively smooth at the atomic level, so as not to interfere with the topography of the sample[82]. The common substrates are glass, graphite and mica.

Glass has irregularities on the nanometer range, however, it is a good substrate for imaging larger samples (e.g. cells) where a nanometer resolution is not required. It also has the advantage of allowing cultures to grow directly on it. The cover slips require careful cleaning to avoid contaminants. Glass has a negative charge in aqueous conditions[35, 82, 89].

Graphite is a nonpolar hydrophobic conducting substrate that consists of hexagonally ordered carbon atoms[89]. It is a poor candidate for experiments with samples that are deposited from aqueous solutions, since the sample will spread poorly on it. However, graphite is still a very popular tool among biological researchers[35, 89, 90].

Mica is the most popular substrate used in AFM experiments[35, 86]. Mica consists of thin, flat crystalline plates that can be cleaved using scotch tape[74]. It provides a surface that is atomically flat over large (micron-scale) areas making it possible to achieve atomic resolution[35, 90]. Mica has a polar surface that makes it highly hydrophilic[82, 89].

2.3.5 Modes of Operation: Contact

Modern AFMs have a number of operating modes that can be selected depending on the experimenter’s needs. The contact mode, also known as the dc mode or constant-force mode[86], is the original AFM imaging mode[78]. The cantilever tip and the sample surface are brought into direct contact, while the surface is scanned by the tip[35, 73], as shown in Figure 2.21. The force between the tip and the surface is held constant using a feedback loop. The scanner moves vertically to maintain a constant “setpoint” cantilever deflection as the surface topography changes[75, 84]. The “setpoint” is the measure of the desired constant force that is chosen by the experimenter.

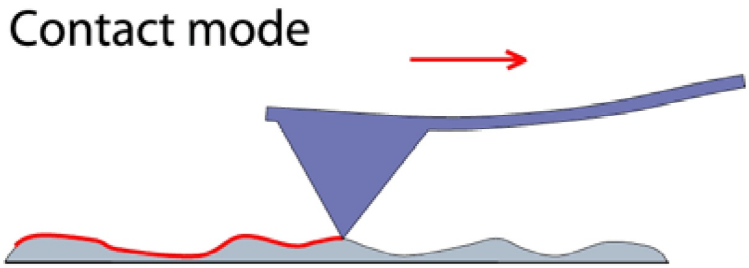

Figure 2.21: Contact mode of operation. The tip of the probe is in contact with the sample surface. The height of the cantilever is adjusted to keep the deflection (i.e. the force) constant[81].

The contact mode can be used in air and in liquid imaging environments[78, 84]. It has the advantage of being simple to operate, however the resultant topographical image is strongly influenced by the tip geometry. It is also not an ideal mode for studying soft biological samples as it can be potentially damaging to the surface[81].

2.3.6 Modes of Operation: Tapping

The tapping mode, also called intermittent contact mode, was invented in 1993[73, 75, 86]. In this mode the surface is scanned by the tip attached to a cantilever that is being oscillated at or near its resonance frequency[84]. The oscillation amplitude of the cantilever is high (20-100nm[84, 91]), which causes the tip to bounce up and down (tap) on the surface (see Figure 2.22)[35, 84]. The repulsive force experienced by the tip causes a reduction in the oscillation amplitude[73]. The feedback loop detects the variation in amplitude and corrects to constant “setpoint” value during the scan. The image is then produced by mapping the vertical distance the scanner moves to maintain the constant amplitude at each (x,y) point[78, 92]. Thus in the tapping mode the amplitude is altered due to the tapping of the surface[91].

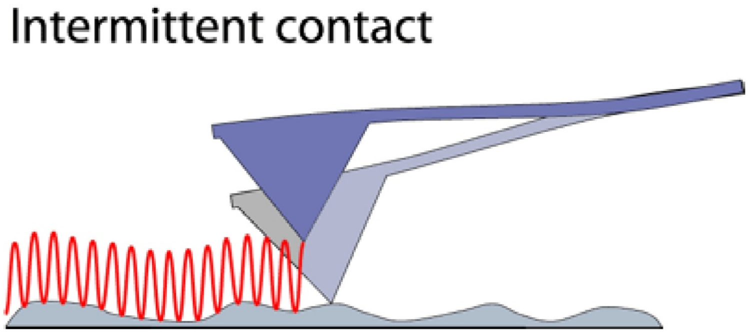

Figure 2.22: The tapping mode of operation. The oscillating cantilever causes the tip to gently bounce on the sample surface[81].

Tapping mode can be used in air and in liquid environments[78, 84]. It requires hard (high force constant) cantilevers that are shorter and thicker and have a high resonant frequency[81, 84]. Tapping mode is well suited for imaging delicate samples, since it has the advantage of a much smaller lateral force (potentially damaging side-to-side pulling) than present in contact mode[81].

2.3.7 Modes of Operation: Phase Imaging

The interaction between the tip and the surface depends not only on topography of the sample but also on its mechanical characteristics (e.g. hardness, elasticity, etc.)[78]. During imaging in tapping mode oscillation of the cantilever is being driven at some frequency. However, when the tip strikes the surface it transfers a small amount of energy to it. The exact amount of energy depends on the sample mechanical characteristics[35, 81]. This energy transfer causes a shift in the phase of cantilever oscillation as compared to the driving signal[82]. Phase images are produced by recording this phase shift during a tapping mode scan[78]. Phase imaging allows different areas to be distinguished on a topographically flat surface, an example is given in Figure 2.23. The topographical imaging with tapping mode and the phase imaging can be performed during the same scan[78].

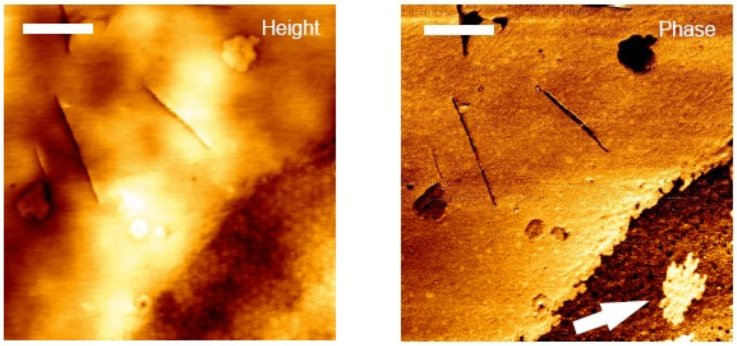

Figure 2.23: An example of the benefit of phase imaging. The topographical (height) image does not show well defined features, probably due to very gentle variation of the height that was not picked up by the topographical imaging. The phase image, however, shows the sharply contrasting regions that could be detected by measuring the phase shift they induced[81].

2.4 Fluorescence Microscopy

Fluorescence microscopy is another method that could be used to image supported monolayers[2, 12, 21, 37, 47]. In fluorescence microscopy, the images are obtained by attaching a fluorescent label (fluorophore[93]) to the sample and then measuring the distribution of fluorescence intensity within the illuminated area[32, 94]. Fluorophores are naturally fluorescent chemical compounds that act as stains and can attach themselves to the sample. They are excited by a specific wavelength of irradiating light and emit light of different (longer) wavelength[93, 94]. In the fluorescent microscope, a filter is used to make sure that only the emitted light reaches the eye (or a detector), resulting in the fluorescent structure being superimposed with high contrast against a dark background.

Fluorescence imaging was part of my original research plan, however, after very careful consideration it was decided not to include any fluorescence experiments into my project. The plan was to use a fluorescently labeled sphingomyelin (SM) to visualize possible domains (topographical features) formed in the sample. In order to prepare for this part of the project, a literature search was performed which revealed several interesting points about the way SM behaves. The structure of SM is given in Figure 2.24.

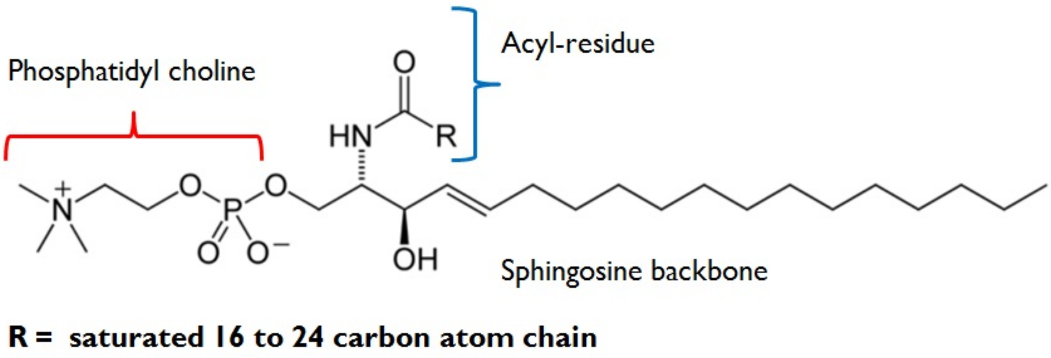

Figure 2.24: General structure of sphingomyelin. The different types of sphingomyelin are distinguished by the number of carbons in the Acyl residue (the R value). The figure is adapted from [95].

When cholesterol (Chol) is present in the sample mixture, SM is located in the liquid-order (L_o) phase domains[96–98], similar to lipid rafts (as was previously mentioned). Bar et al. used a number of techniques to show that on its own SM tends to be in gel phase at room temperature[99], a finding confirmed by other studies[96–98, 100, 101]. However, they also discovered that different types (depending on the R value) of SM exhibit slightly different phase behavior (manifesting in different types of gel phase)[99]. It has also been shown that SM resembles DPPC in its behavior, specifically showing similarities in head group structure, chain length (R16-SM), transition temperature, and orientation in bilayers[95, 102]. Figure 2.25 shows the structure of R18-SM (used in my project) and DPPC for comparison.

The behavior of a fluorescently-labeled SM, however, appears to be different from pure SM. Baumgart et al. conducted an extensive study of phase preferences of fluorescently labeled species[103]. They demonstrated that Bodipy-labeled SM prefers the fluid phase. In addition, they showed that, in general, when the label is attached to the carbon chain (the tail) of a lipid, it will prefer to be in fluid phase[103]. They hypothesized that addition of the label to the tail adds bulk to the structure, thus reducing the packing order of the lipids. This hypothesis was confirmed by Shaw et al. when they showed that SM labeled with Bodipy and NBD prefers to be in fluid phase[101]. They demonstrated that addition of a label reduces the affinity of the lipid for more ordered domains[101]. The phase altering effect of fluorescent labels are not unique to SM. The studies mentioned here all caution against using labels for experiments that depend on lipid phases, as the labeled species do not retain the original phase characteristics of the pure ones[47, 96, 97, 101, 103, 104].

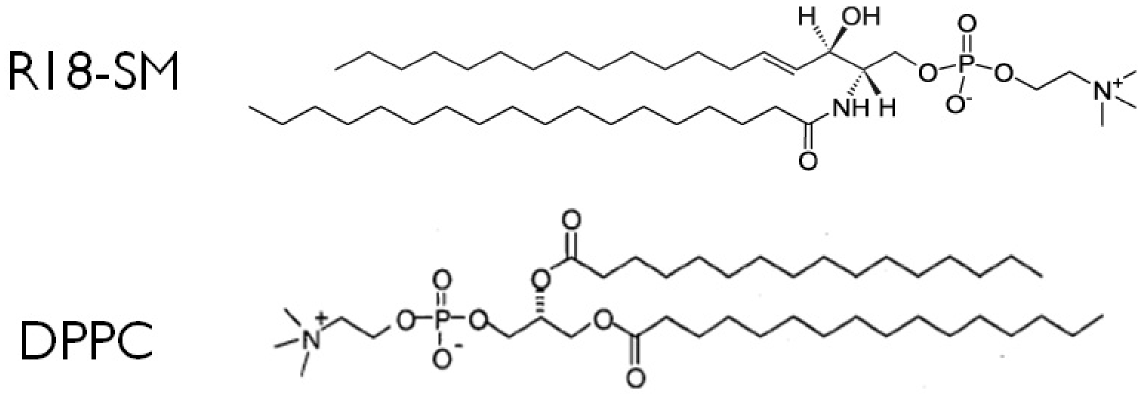

Figure 2.25: Structure of R18-SM vs structure of DPPC[41]. It has been shown that SM and DPPC exhibit a number of behavioral similarities[95, 102].

These facts are very important in terms of relevance to my project. It was originally decided to use Topfluor (a type of Bodipy[105]) to label SM in my samples. Topfluor attaches to the tail of SM, which would most likely cause SM to be in fluid phase instead of gel phase. This posed a problem for my project. The purpose of my study was to find a combination of lipids, such that, while mimicking neuronal membrane composition, they will produce a monolayer rich in topographical domains for further study with relation to Aβ. The domains are produced due to the nature of phase behavior of the lipids. It was expected that the presence of SM will encourage domain formation, which depends on the phase of SM. Since fluorescent labeling appears to alter the domain-forming property of lipids (namely, the phase), it was decided not to proceed with fluorescent microscopy experiments.

Chapter 3

Experimental Methods

3.1 Choice of Lipids

For the purposes of my project, I selected five lipids that seemed the most relevant to mimicking neuronal membrane, as well as the studies of Aβ behavior and membrane heterogeneities due to domain formation. These lipids are: 1-palmitoyl-2-oleoyl-sn-glycero-3-phosphocholine (POPC), 1-palmitoyl-2-oleoyl-sn-glycero-3-phosphoglycerol (POPG), cholesterol (Chol), sphingomyelin (SM), and ganglioside GM1 (GM1). The structures of these lipids are shown in Figure 3.1. I chose POPC because it appears to be the most common lipid in neuronal membrane[106]. In addition, POPC was used in a number of studies of lipid rafts and Aβ binding[3, 4, 21, 28, 48, 62, 107], which are both related to the future applications of this project. I decided to include POPG in my samples, because it has been shown that the presence of POPG in the sample leads to accelerated Aβ fibril formation[14]. To my knowledge, POPG was not yet incorporated into any atomic force microscopy studies of model lipid monolayers, however, several studies did use it with relation to amyloidogenic peptide behavior[3, 14, 28]. The choice to include Chol into my sample set is explained by the fact that Chol is one of the prominent components of neuronal membranes[5, 8, 49, 60, 61, 63]. Additionally, it is one of the key components of lipids rafts, the importance of which to Aβ fibrillization was detailed in the introductory Chapter

1 and the theoretical Chapter 2. Chol has also been shown to strengthen the Aβ - membrane interaction[5, 19]. Chol was used in a number of studies that looked into raft and domain formation[22, 45, 51, 52, 107]. SM is the other key components in raft composition and is also present in neuronal membrane[5, 6, 9, 49, 60, 61, 63, 108]. Several studies of lipid rafts and Aβ behavior incorporate SM[22, 37, 38, 45, 46, 48, 52, 62, 107]. I chose to use GM1 to represent the presence of gangliosides in neuronal membrane[6, 10, 49, 61]. GM1 in particular has been shown to promote binding of Aβ to the membrane[6, 8, 14, 27]. GM1 has also been used in modeling the composition of lipid rafts[44]. This particular ganglioside appears to be the most popular choice for investigations of Aβ behavior[1, 5, 21, 22]. It has been shown that GM1 in combination with Chol enhances the interaction between Aβ and the membrane[5].

Table 3.1 summarizes the samples that I investigated during my project. The table also lists the proportions (by weight) in which the lipids were combined and the references on which the proportions were based.

3.2 Experimental Procedure

Three of the lipids used for the project, 1-palmitoyl-2-oleoyl-sn-glycero-3-phosphocholine (POPC), 1-palmitoyl-2-oleoyl-sn-glycero-3-phosphoglycerol (POPG), ganglioside GM1 (GM1) were purchased from Avanti Polar Lipids (Alabaster, AL) in powder form. The other two lipids, cholesterol (Chol) and sphingomyelin (SM) were purchased from Sigma-Aldrich (St. Louis, MO), also in powder form. The lipids were dissolved in chloroform with 1 mg/mL concentration. The sample mixtures where then prepared with the proportions given in Table 3.1, by weight.

Samples with the model monolayers were prepared on a Langmuir-Blodgett trough (NIMA 601M, Coventry, UK) using Milli-Q water as the subphase. The lipid solutions in chloroform were spread on the subphase surface with a syringe. After 10 minutes the solvent (chloroform) evaporated and the lipids had time to spread out on the surface. The monolayers were compressed to the target pressure of 35 mN/m and deposited on a freshly cleaved mica using vertical deposition with the dipping speed of 10 mm/min. Prior to deposition, pressure-area isotherms were collected for every sample mixture to ensure that the collapse pressure exceeds the deposition target pressure, eliminating the possibility of the monolayer collapse during deposition process.

AFM imaging was carried out on the JPK NanoWizard II (JPK Instruments AG, Germany) mounted on Olympus 1X71 inverted optical microscope, as shown in Figure 2.14b, in intermittent contact mode in air. Several tips were tried, with the best results given by the silicone AIST-NT fpN11 tips (spring constant in 2.6-9.8 N/m range, resonant frequency in 118-190 kHz range). Images (512×512 pixels) were scanned at a line rate of 0.5 Hz. Imaging parameters were optimized for the best possible quality, unique to each sample. When not in use, all samples were stored in a glass desiccator in individual petri dishes sealed with Parafilm.

Images were processed using JPK Data Processing software version spm-4.0.23 (JPK Instruments AG, Germany). Images were leveled using the Linefit function of Degree 2 from the software: each scan line was fitted with a polynomial fit, which was subsequently subtracted from the data. This was done to correct for the "background" height changes[109]. Occasionally, the Remove Lines operation was used to replace streaks in the image with the average between the neighboring scan lines. The streaks are usually caused by the tip sticking and then pulling off the surface[109]. A Gaussian smoothing was performed using the Low-pass function (Sigma: 1.000) in order to enhance the features on the images and reduce the noise. Statistical data was obtained using the Cross-Section tool and collecting 100 measurements for pore depth and domain height. The average value and standard deviation were then calculated.

Further statistical analysis of the images that exhibited pore formation was done using SPIP software version 5.1.6 (Image Metrology). The images were leveled using Line-wise correction option, where LMS fit method of order 2 was used. Sometimes specific cross-sections were corrected to eliminate streaks between lines. The Histogram function was then used to determine the height distributions of topographical features and the area (percentage) occupied by pores. A Gaussian smoothing with standard deviation of 1 was then performed to reduce the noise and enhance the features in the images[110]. Subsequently, Particle and Pore Analysis function was used to detect pores and determine their length and breadth (width). The step-by-step procedure outlined here is given in the Appendix.

Table 3.1: The list of samples under investigation during the course of the project. Included are the references on which the sample compositions and proportions were based.

Sample	Proportion	Reference
POPC	Pure (100%)	[3, 4, 21, 28, 60]
POPG	Pure (100%)	[3, 14, 28]
POPC	Pure+20% Chol	[4, 5, 19, 60, 63]
POPG	Pure+20% Chol	[5, 19, 63]
POPC/POPG	60:40	[2, 3, 28]
POPC/POPG	60:40+5% Chol	[3, 5, 19, 28, 63]
POPC/POPG	60:40+20% Chol	[3, 5, 19, 28, 63]
POPC/POPG/SM	40:40:20	[3, 6, 63]
POPC/POPG/SM	40:40:20+5% Chol	[3, 5, 6, 19, 63]
POPC/POPG/SM	40:40:20+20% Chol	[3, 5, 6, 19, 63]
POPC/SM/Chol	75:2:23	[5, 6, 19, 33, 37, 38, 46, 48, 49, 52, 60, 62, 63, 107]
POPC/SM/Chol	75:20:5	[5, 9, 19, 37, 38, 46, 48, 52, 62, 63, 107, 108]
POPC/SM/GM1/Chol	74:2:1:23	[5, 6, 8, 10, 19, 21, 22, 27, 33, 38, 44, 61, 63]

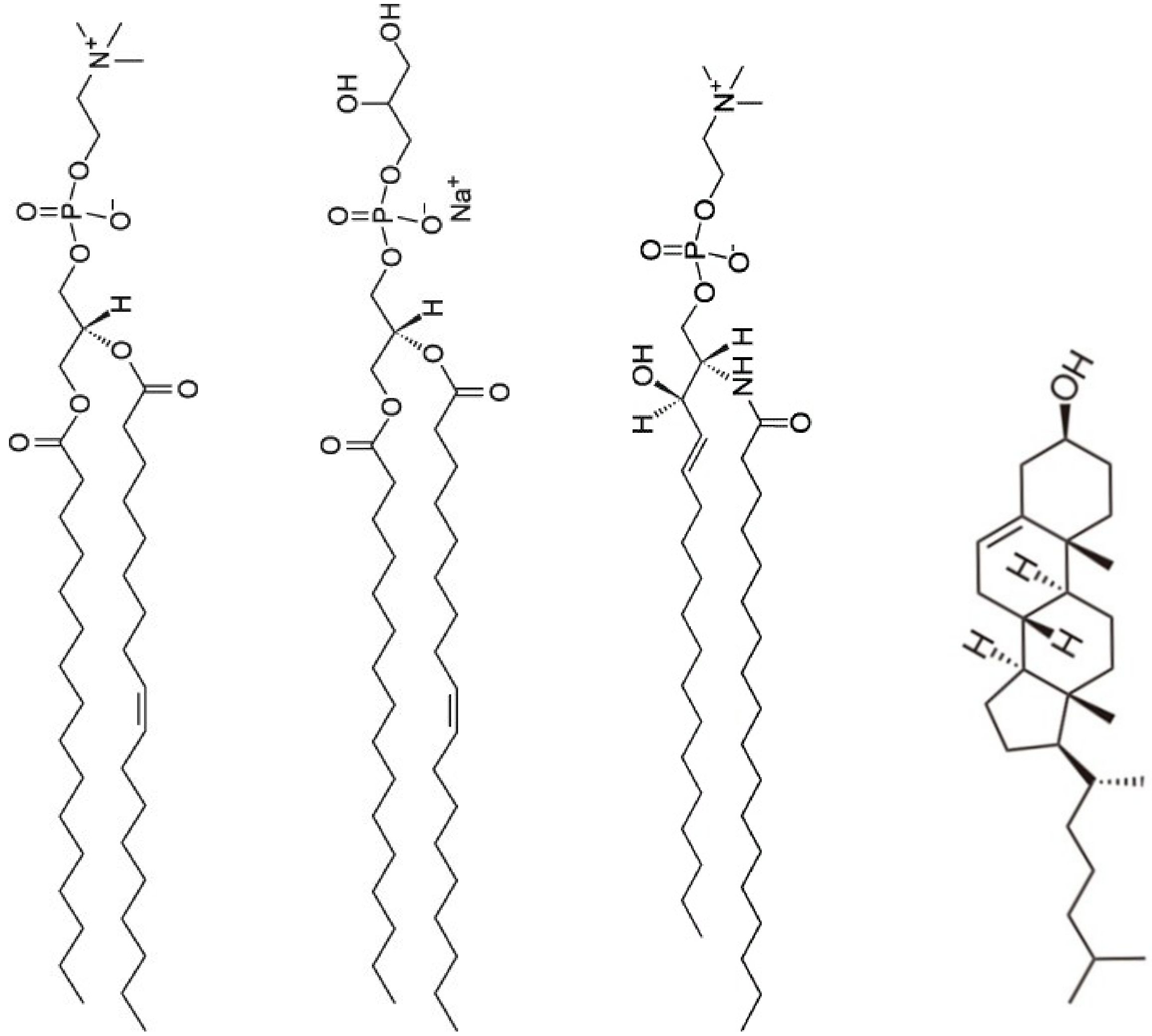

a) POPC b) POPG c) SM d) Chol

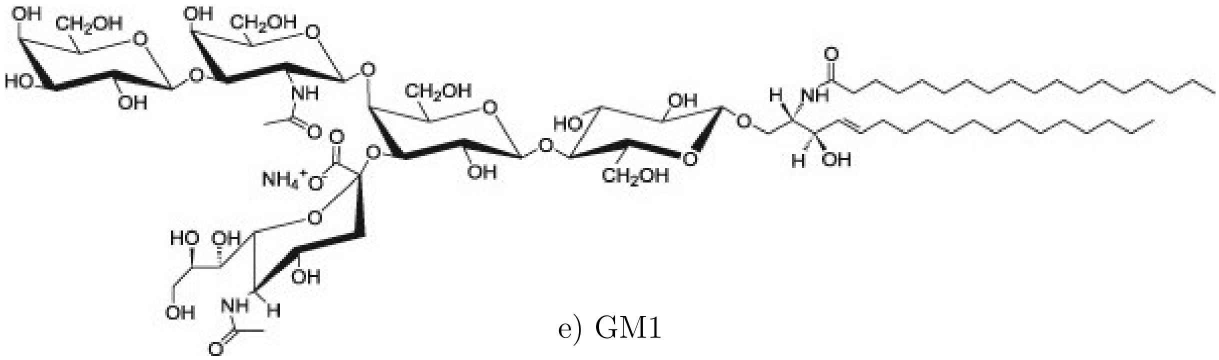

e) GM1

Figure 3.1: The structures of the lipids used in my project: a) POPC[111], b) POPG[112], c) SM[113], d) Chol[114], and e) GM1[115].

Chapter 4

Experimental Results and Discussion

4.1 Langmuir-Blodgett Experiment: Pressure-Area Isotherms

The purpose of collecting pressure-area isotherms is to determine if the collapse pressure for sample monolayers is greater than the deposition pressure of 35 mN/m. If collapse pressure exceeds the deposition pressure then the monolayer will collapse during the deposition process. The deposition pressure of 35 mN/m was chosen because it corresponds to the pressure found in natural lipid membranes, as was mention in Chapter 2. Therefore, the isotherms are used to check if a given lipid combination can be used as a monolayer sample for my project. Fortunately, all of the samples have a collapse pressure well above 35 mN/m. The collected isotherms are given in Figure 4.1.

A far more comprehensive isotherm for the purposes of studying properties of the monolayers is a pressure-molecular area isotherm[68]. A molecular area isotherm is a unique characteristic of the molecules making up the monolayer film, hence would be very useful for the purposes of comparing my isotherms to those available in literature. However, according to the manufacturer[116], it is impossible to construct such an isotherm for a mixture of more than two lipids using the L-B trough available to us. If it was attempted, then no real meaningful information could be extracted from it. Therefore, for the sake of consistency, I decided to collect only pressure-area isotherms for all my samples.

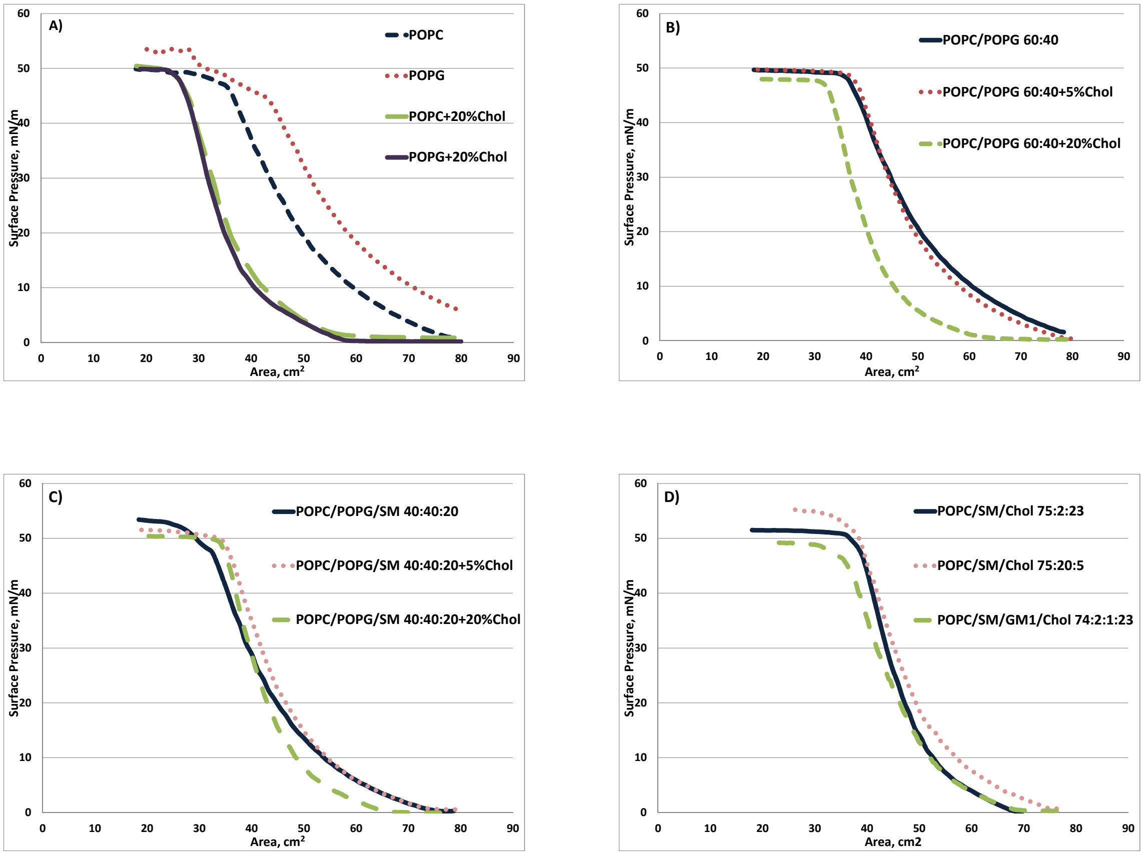

Figure 4.1: Pressure-area isotherms collected for the sample mixtures given in Table 3.1: a) Control sample mixtures; b) POPC/POPG mixture with 5% and 20% Chol, c) POPC/POPG/SM mixture with 5% and 20% Chol, d) POPC/SM/Chol in different proportions with added GM1. Note that all the collapse pressures are well above 35 mN/m.

It appears that an addition of 20% Chol to POPC and POPG results in the isotherm shifting, as seen in Figure 4.1a. The same trend is observed in Figure 4.1b, when 20% Chol is added to a mixture of POPC/POPG. However, it is not seen for the case of POPC/POPG/SM in Figure 4.1c. It seems that for both systems in Figure 4.1c and Figure 4.1d addition of Chol or changing quantity of other lipids does not have any significant effect, resulting in isotherms that closely resemble each other.

In terms of literature comparison, I could not find any isotherms for mixtures of the same composition as my samples. The isotherms available for pure POPC and POPG all confirm that the collapse pressure of these lipids is well above 35 mN/m[117–121]. Note that the bump, which is not seen in literature[118, 119], in the POPG isotherm in Figure 4.1a is most likely due to leakage of the trough, rather than to anomalous behavior of the lipid. The isotherms available for the mixture of POPC/SM/Chol confirm the trend seen in Figure 4.1d, that changing the amount of SM and Chol and adding GM1 does not have a significant effect on the shape of the isotherms[122]. However, it is difficult to draw any more concrete comparison since the proportions of lipids used in [122] are very different than those in this project.

Collecting the pressure-area isotherms revealed that, based on comparing POPC and POPG results with literature, the obtained graphs can be trusted, which is crucial for the mixtures for which the literature comparison is not possible. Isotherms were obtained to characterize new sample mixtures, such as POPC/POPG/SM ones. Additionally, the isotherms served as a test to ensure that the no anomalies occur at 35 mN/m and this pressure can be reached for all mixtures, making it possible to proceed with the AFM part of the project.

4.2 Atomic Force Microscopy Experiments

Atomic force microscopy was used to investigate a number of mixtures (listed in Table 3.1) to determine if they could be used as a model for neuronal membrane for further studies of the effect of topographical heterogeneity on Aβ behavior. During AFM imaging two types of topographical features were observed: domains and pores. It is important to clarify the distinction between them. Domains are topographical features that are formed due to the sample properties, such as phase, composition, etc. Pores are an experimental artifact and do not represent any information about the topography of the sample surface. This is illustrated in Figure 4.2. The domain height values that are quoted further on in this section refer to the height difference between lower and higher domains, as shown in Figure 4.2 (similarly the depth values for pores). The goal of the experiment was to determine a lipid composition that, while mimicking neuronal membrane, exhibits formation of prominent domains.

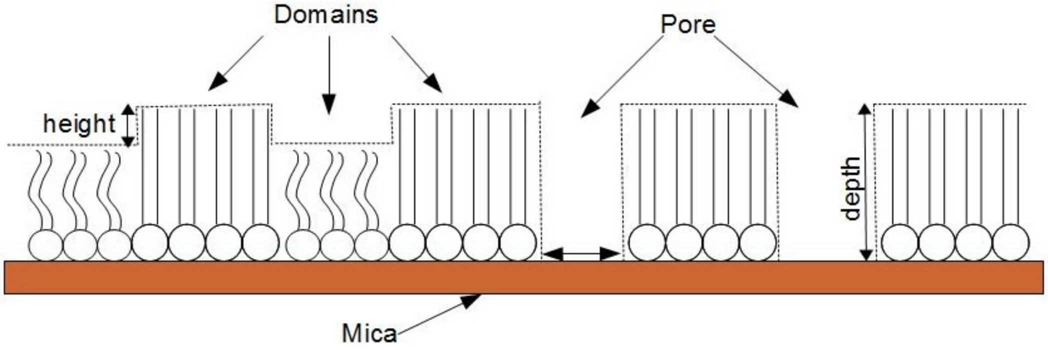

Figure 4.2: A schematic diagram of a supported monolayer exhibiting both domains and pores. The dotted line represents the sample cross-section.

4.2.1 Control Samples

In order to understand heterogeneity formation in lipid mixtures, first the topography of the lipids should be investigated. For that purpose there are four control samples in my project: pure POPC monolayer, pure POPG monolayer, POPC+20% Chol, and POPG+20% Chol. The addition of cholesterol is required to test its effects on the pure lipids. The representative $2\mu m \times 2\mu m$ topographical images of results obtained for POPC and POPC+20% Chol are given in Figure 4.3, also included are examples of phase images. The $2\mu m \times 2\mu m$ topographical images of POPG and POPG+20% Chol are shown in Figure 4.4. It is clear from Figure 4.3a and Figure 4.4a that both POPC and POPG tend to form a porous topography, rather than a uniform one that was expected for the case of single-lipid monolayer. Aside from the pores, the POPC and POPG monolayers also exhibit some roughness.

In the case of pure POPC, calcucations revealed that the average depth of the pores is approximately 2.20 ± 0.56 nm. This number suggests that the pores in the images extend through the entire thickness of the monolayer. According to Kepczynski et al. the theoretical size of a POPC bilayer is around 3.49 nm, which would mean that the size of a monolayer is approximately 1.75 nm[123]. This value seems to be roughly on the same order as the depth of the holes in the POPC monolayer that I observed in my samples. A more thorough comparison is not possible since Kepczynski et al.'s study was a theoretical simulation of a hydrated bilayer, which is different from the environment of my sample. Unfortunately, they did not provide any uncertainty for their value of the bilayer thickness. The POPC monolayer exhibits some roughness, with the features mesuread to be approximately 0.21 ± 0.10 nm in height and 32.35 ± 11.06 nm in widht.

Addition of 20%Chol to POPC appears to result in a more uniform surface coverage with no pore formation. However, even though the cross-section in Figure 4.3f does not look flat, the features that are formed are very small with a height of 0.17 ± 0.07 nm, which is barely above the expected height deviations from background noise, and a width of 35.81 ± 14.78 nm.

The pure POPG monolayer revealed a topography similar to the POPC one, only with less-pronounced pores. The average depth of the pores was found to approximately be 1.05 ± 0.35 nm. This value suggests that the pores visible on the image do not extend all the way to the mica substrate. Kucerka et al. showed that the thickness of a POPG bilayer is 3.67 ± 0.07 nm, which gives a monolayer thickness of 1.835 ± 0.035 nm[124]. The pore depth from my sample is approximately half of this thickness value. The surface features observed for POPG have an approximate height of 0.36 ± 0.14 nm and width of 69.25 ± 14.32 nm. This suggests that POPG forms more prominent features than POPC does. As with POPC, addition of 20%Chol appears to provide a smooth uniform coverage with no pores. The features in POPG+20%Chol are slightly higher and thinner than those for POPC+20%Chol having a height of 0.20 ± 0.18 nm and a width of 27.77 ± 8.51 nm. However, the height difference between the high and low features seem to be varying, producing the large value for standard deviation.

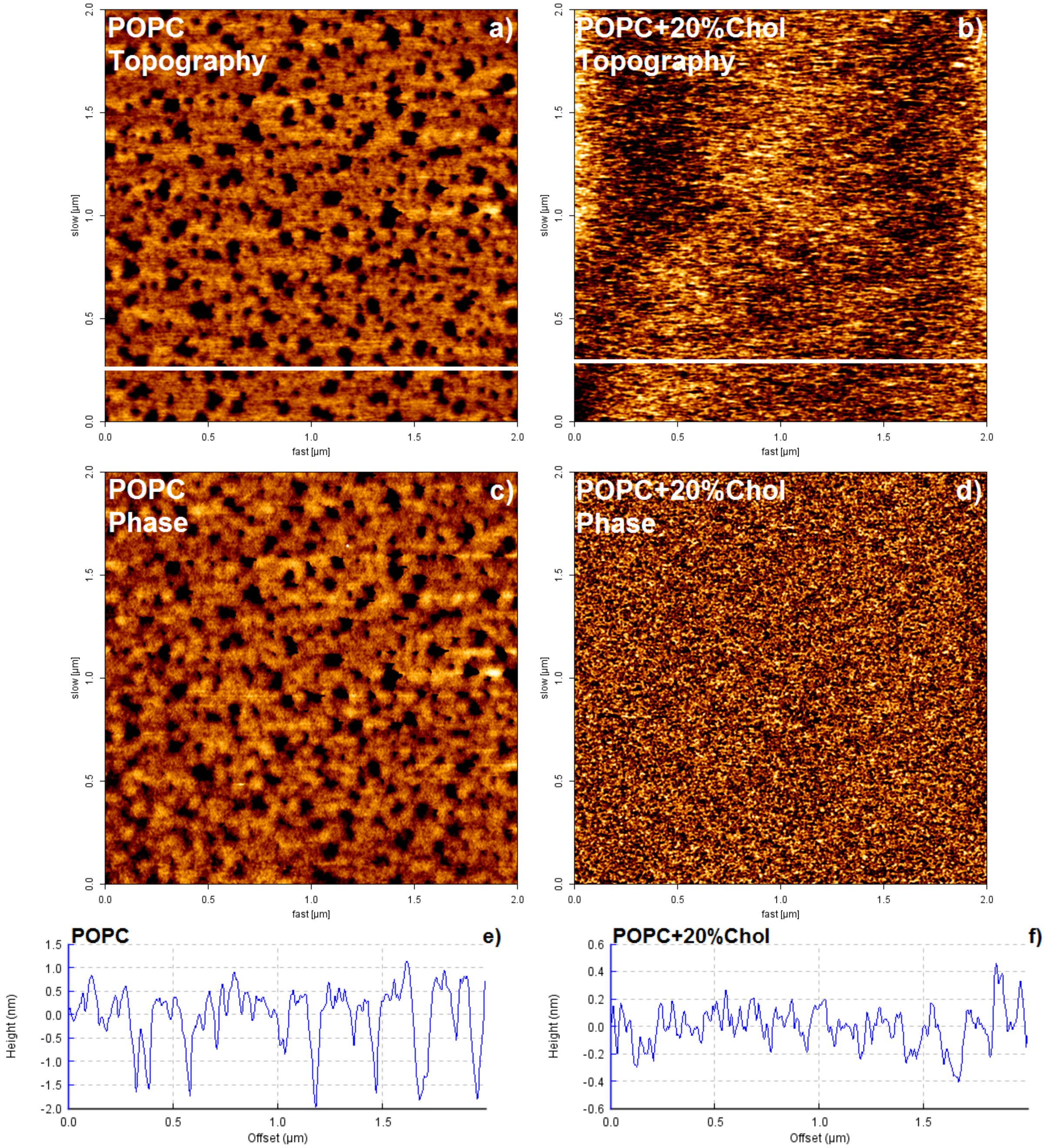

Figure 4.3: The AFM images of the control sample of pure POPC and POPC+20%Chol. a) The topographical image of pure POPC monolayer. b) The topographical image of POPC+20%Chol monolayer. c) The phase image of POPC monolayer. d) The phase image of POPC+20%Chol. e) A cross-section of POPC monolayer along the line in image a). f) A cross-section of POPC+20%Chol along the line in image b).

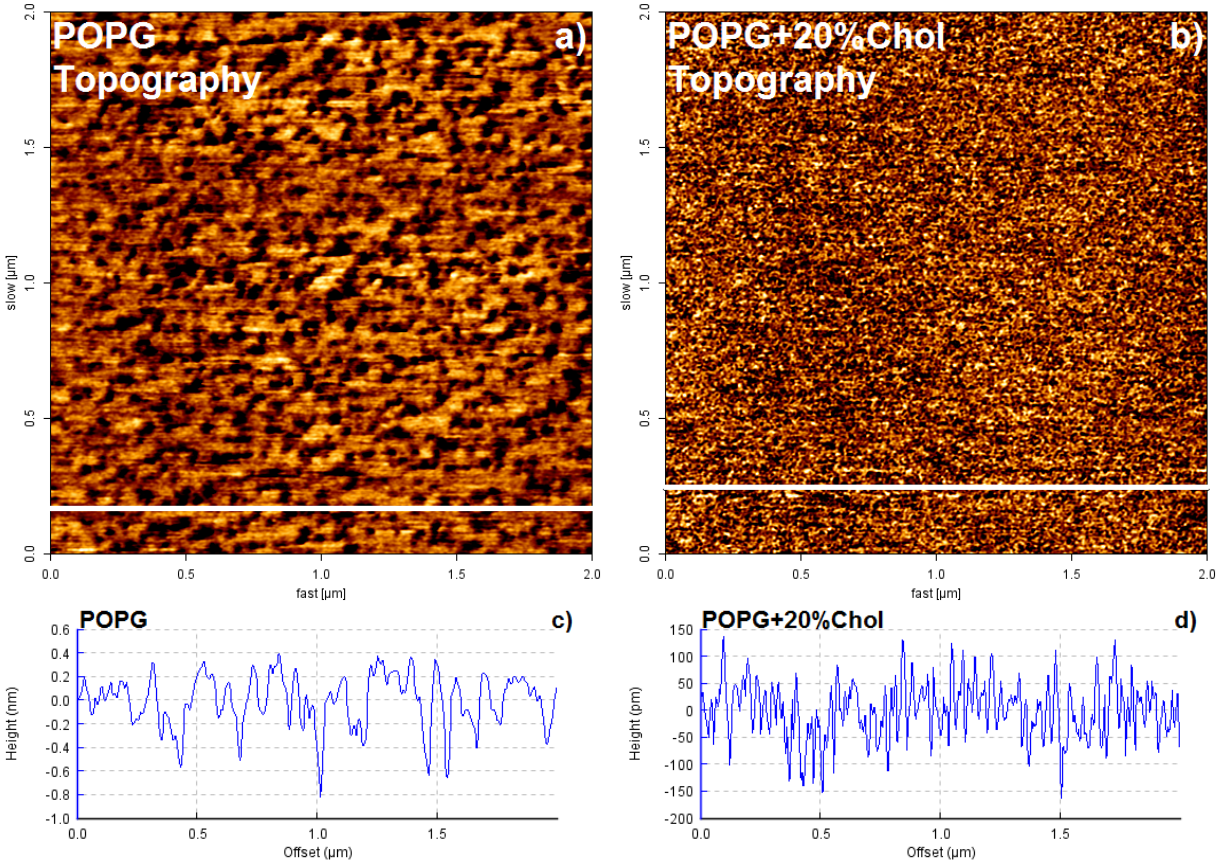

Figure 4.4: The AFM images of the control sample of pure POPG and POPG+20%Chol. a) The topographical image of pure POPG monolayer. b) The topographical image of POPG+20%Chol monolayer. c) A cross-section of POPG monolayer along the line in image a). d) A cross-section of POPG+20%Chol along the line in image b).

The possible reasons for the pore formation observed in the case of both POPC and POPG monolayers are elaborated on in the Discussion section later on. Let it be noted that the pores appear very pronounced on the images in Figure 4.3a and Figure 4.4a because the images are taken on such a small scale ($2\mu\text{m} \times 2\mu\text{m}$). Figure 4.5 provides the $10\mu\text{m} \times 10\mu\text{m}$ images of the POPC and POPG monolayers for comparison.

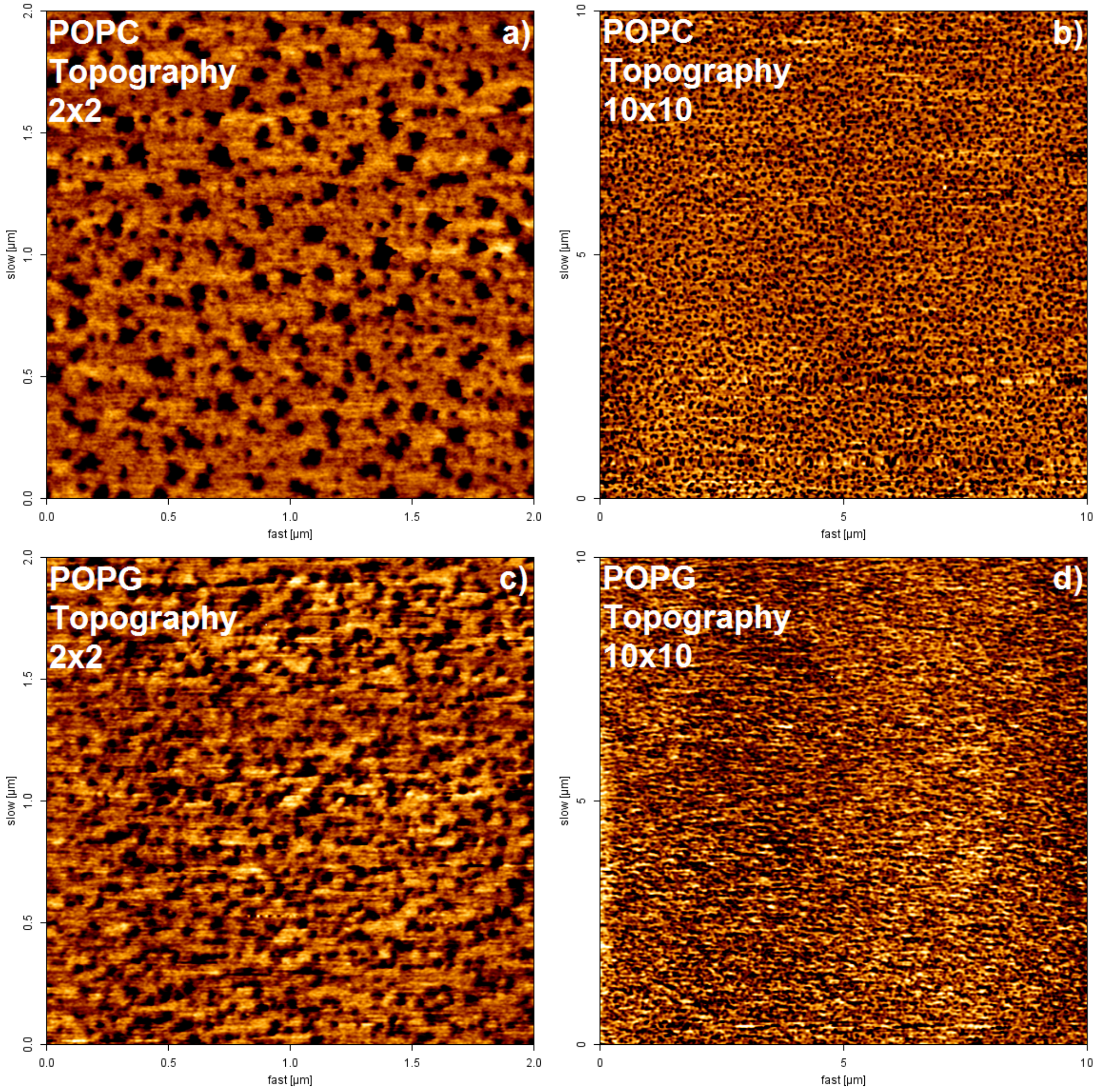

Figure 4.5: The $2\mu m \times 2\mu m$ and $10\mu m \times 10\mu m$ AFM images of the control sample of pure POPC and POPG. The pores are less pronounced on a larger scale, specially in the case of POPG. a), b) The topographical image of pure POPC monolayer. c), d) The topographical image of pure POPG monolayer.

4.3 POPC/POPG 60:40

The combination of POPC/POPG 60:40 does not exhibit the same porous topography as its separate constituents, as can be seen in Figure 4.6a. Domain formation is visible, specially in the phase image (image not shown). Unfortunately phase images cannot be used to draw conclusions regarding sample topography, but it does serve to confirm the presence of domains. Their average height was found to be approximately 0.26 ± 0.08 nm, which is less than those of either POPC or POPG reported in the previous section. The average width, however, is on par with that observed for POPG: 61.28 ± 9.88 nm. The lack of higher domain formation could be possibly attributed to the fact that both POPC and POPG have the same fluid phase[62, 119], however, that appears to contradict the above finding that separately they do form slightly higher structural features. Another possible explanation is that both POPC and POPG are very similar in height, as was mentioned in the previous section, therefore when combined together they are difficult to distinguish with a tool designed for height measurements (AFM). This would also explain why domains are visible in the phase image (image not shown), as phase imaging does not depend on the height of the samples (see Chapter 2, section 2.3.7).

More pronounced domains, however, appeare to be forming when 5% Chol is added to the sample (Figure 4.6b). Their average height and width was found to be approximately 0.36 ± 0.09 nm and 64.51 ± 11.93 nm, respectively. A few pores are also observed to be forming when 5% Chol is added, but not enough to make a proper statistical calculations. The 10μm × 10μm image given in Figure 4.7 shows the topography on the larger scale, where both pores and domains are not prominent.

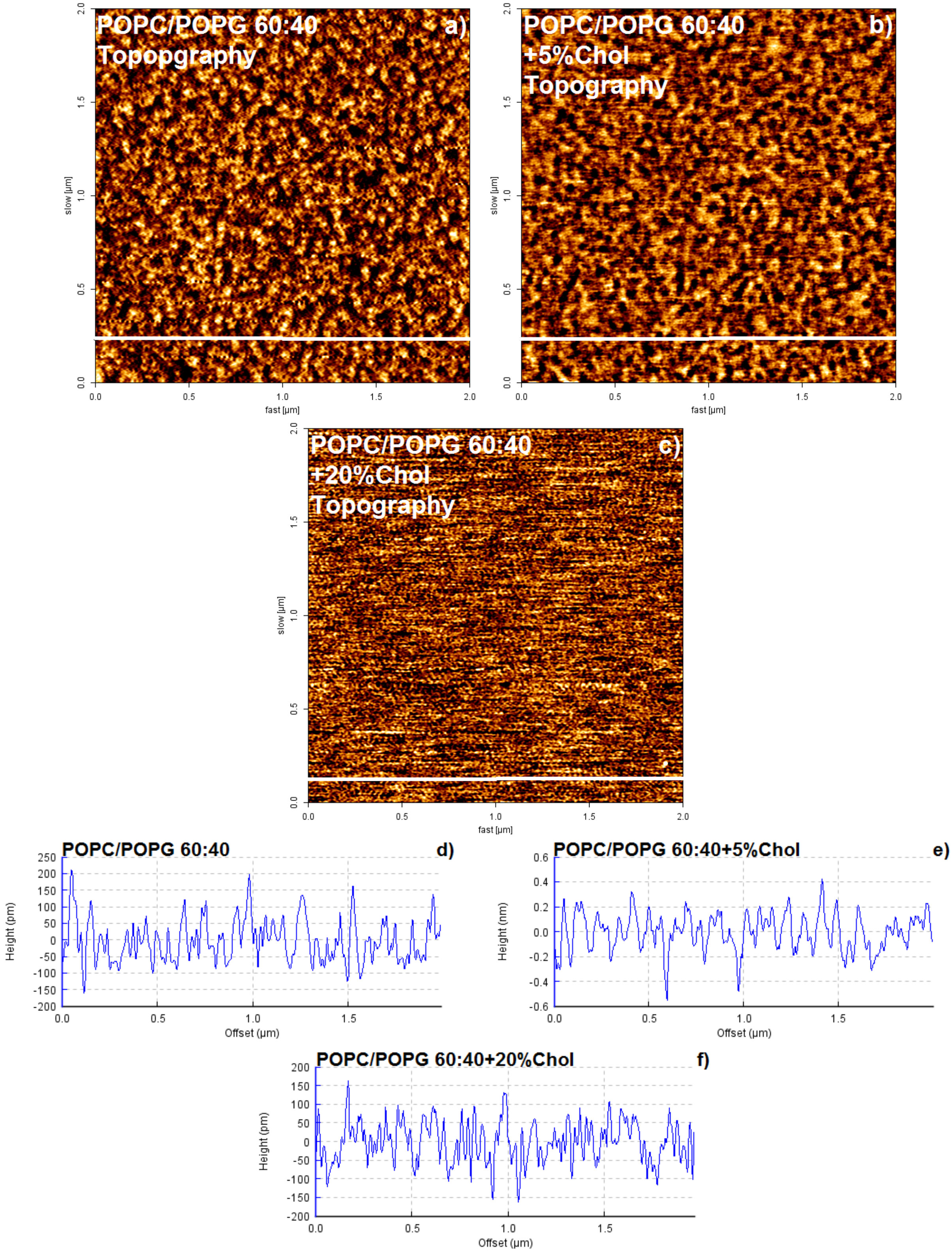

Figure 4.6: The AFM images (topographical and cross-section) of the POPC/POPG 60:40 (a, d) with 5% (b, e) and 20% Chol (c, f), respectively.

Consistent with results from the control samples, addition of 20% Chol caused formation of smooth topography (Figure 4.6c) with no pores. The surface features appear to be very small with the height of 0.26±0.007 nm and width of 28.30±7.42 nm. The height values are the same as value as for the POPC/POPG 60:40 sample, but the widths are a lot smaller than in the case of POPC/POPG 60:40 sample. Therefore, the addition of such a quantity of Chol does not seem to result in formation of more pronounced features than those seen without the 20%Chol in terms of height, the width of the features is less pronounced than in the case with no Chol.

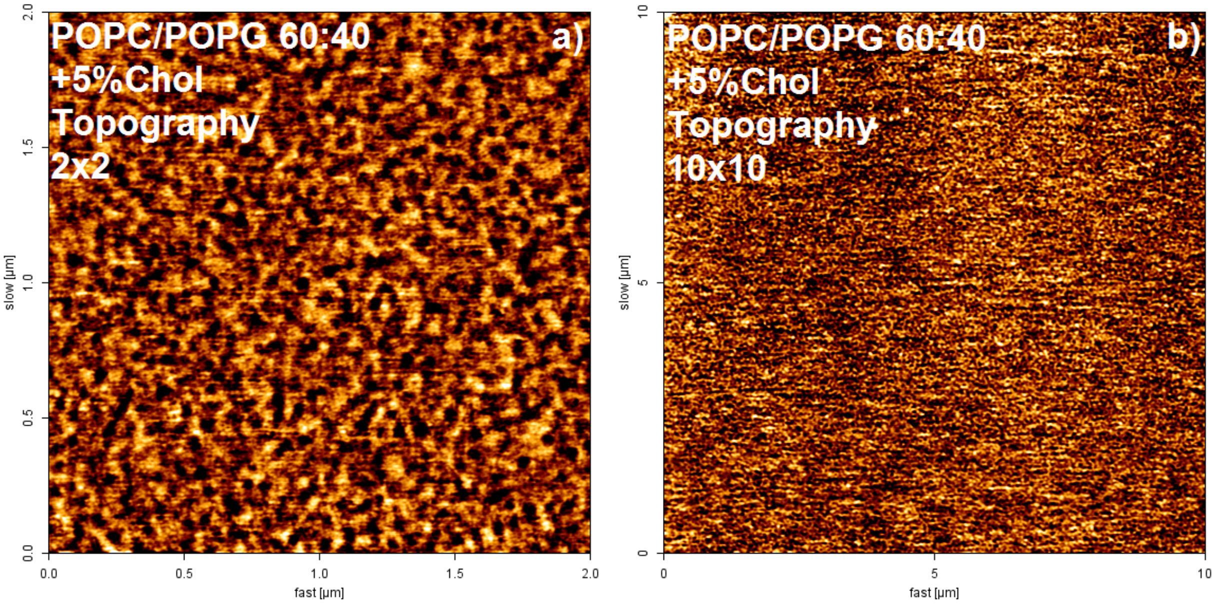

Figure 4.7: The comparison between $2\mu m \times 2\mu m$ (a) and $10\mu m \times 10\mu m$ (b) AFM images of POPC/POPG 60:40 with 5% Chol.

4.4 POPC/POPG/SM 40:40:20

Results for the POPC/POPG/SM 40:40:20 with 5% and 20% Chol are given in Figure 4.8, examples of representative phase images are also included. Similarly to POPC/POPG 60:40 system, POPC/POPG/SM 40:40:20 mixture does not display very prominent topographical features. Their existence, however, is confirmed with the phase image, which does reveal more features as it did for POPC/POPG 60:40, as can be seen in Figure 4.8b. The features have an average height of approximately 0.21 ± 0.05 nm and width of 36.68 ± 6.33 nm. No pores are observed in the case of this sample.

Addition of 5% Chol to POPC/POPG/SM 40:40:20 results in formation of well-defined and prominent domains, as seen in Figure 4.8c,d. It appears that addition of only SM to a mixture of POPC and POPG is not enough to cause formation of high domains, but combined with 5% Chol domains are more pronounced than the features for the case of POPC/POPG 60:40+5%Chol. Their average height was approximately measured as 0.58 ± 0.15 nm and width as 69.79 ± 10.07 nm. The depth of the observed pores is 1.14 ± 0.17 nm. The pores are sufficiently small to be barely noticeable on a larger scale, as shown in Figure 4.9.

Adding 20% Chol caused the pores to break up, leaving a uniform topography (Figure 4.8e,f), similar to that observed in the previous samples. However, the height deviations on the features of this sample is comparable with the background noise, therefore the presence of domains cannot be fully confirmed by looking only at the topographical image. The phase image reveals some structures that could be domains, which would mean that they are formed but are simply too small to be distinguishable.

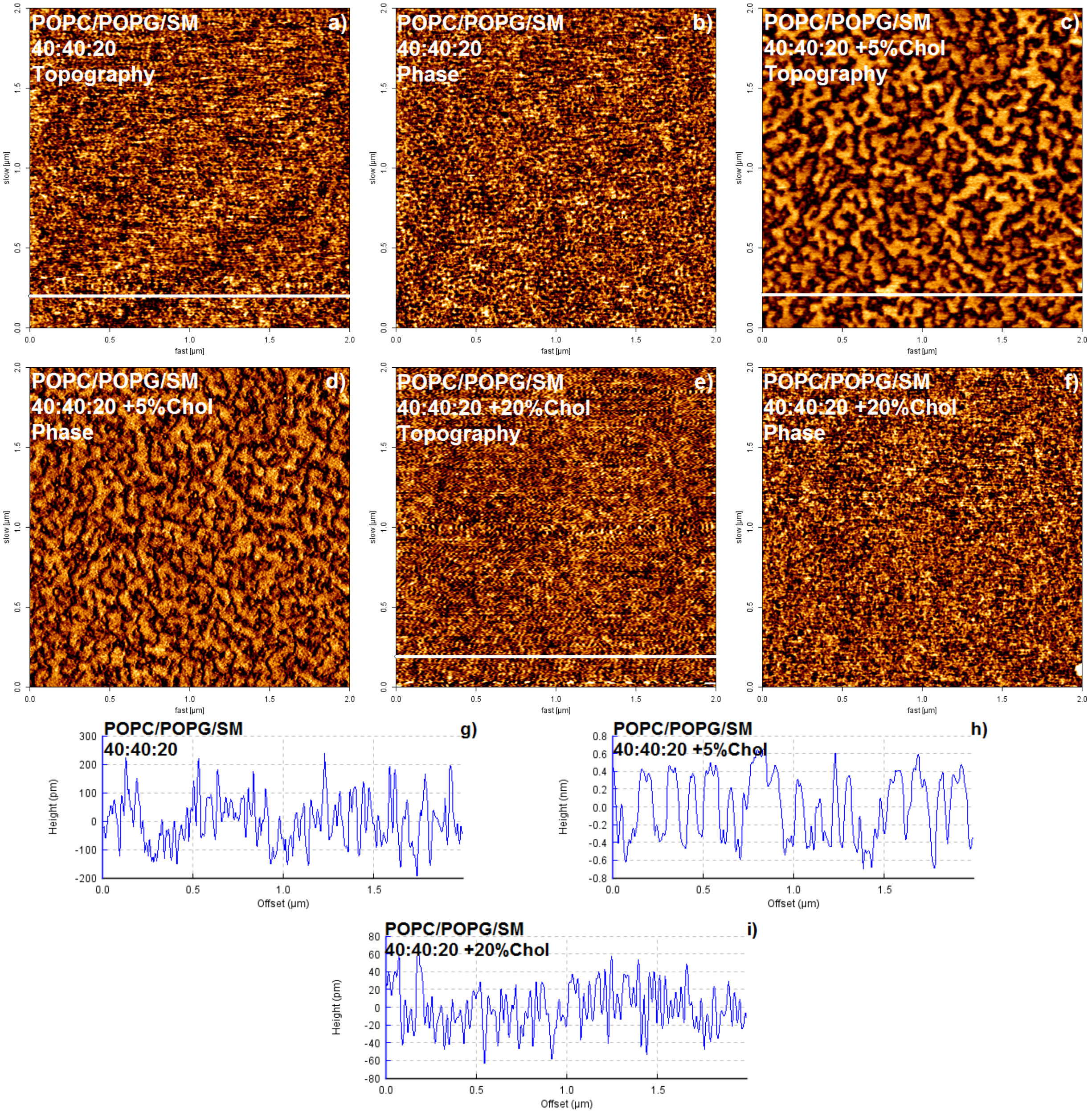

Figure 4.8: The AFM images (topograhical, phase and cross-section) of the POPC/POPG/SM 40:40:20 (a, b, g) with 5% (c, d, h) and 20% Chol (e,f,i), respectively.

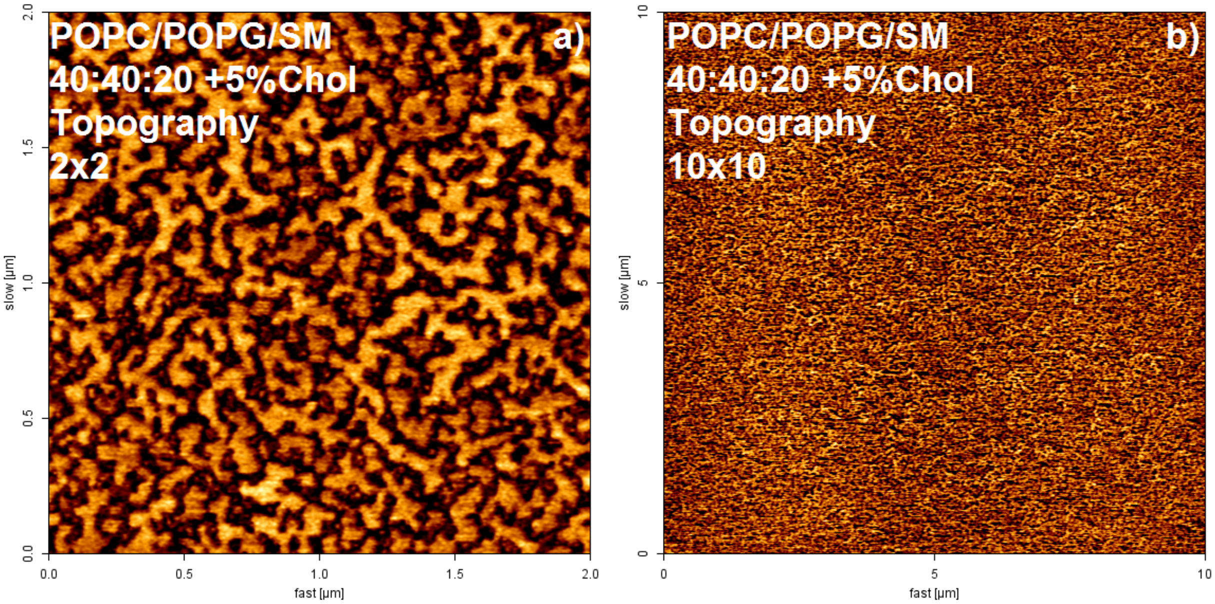

Figure 4.9: The comparison between 2μm × 2μm (a) and 10μm × 10μm (b) AFM images of POPC/POPG/SM 40:40:20 with 5% Chol.

4.5 POPC/SM/Chol

The mixture of POPC/SM/Chol 75:2:23 does not exhibit very prominent features, as seen in Figure 4.10a,b. The average height of the features is approximately 0.16 ± 0.06 nm and width is 30.60 ± 4.46 nm. Addition of SM seems to produce features that, even though still small, can be distinguished from background noise. It appears though that there is not enough SM in this mixture to counteract the tendency of larger quantities of Chol to produce features of very small height, as was observed in the control samples. In order to test this hypothesis, the proportions were changed to POPC/SM/Chol 75:20:5. The resulting images, given in Figure 4.10c,d, confirm this assumption. Domains and clearly visible on the images. Their average height is approximately 0.61 ± 0.12 nm, which means these are the highest domains observed so far. Their average width was measured as 63.21 ± 12.24 nm. Pores are also produced in this sample, which is very clearly seen in the phase image. This appears to be consistent with previous observation of pore formation at similar Chol concentration for the POPC/POPG 60:40 and POPC/POPG/SM 40:40:20.

The average depth of the pores is approximately 1.33 ± 0.22 nm. These pores are big enough to be very noticeable on a larger scale, as can be seen in Figure 4.11.

The addition of GM1 to the original combination (POPC/SM/GM1/Chol 74:2:1:23) results in formation of very pronounced pores (Figure 4.10e,f[1]). It appears that the presence of a large quantity of Chol this time is insufficient and does not produce smooth pore-less topography. The average depth of the pores was measured as approximately 2.30 ± 1.07 nm, which means that the pores in the sample extend all the way to the mica surface. The pores are very pronounced even on a larger scale image, as shown in Figure 4.12. The height of the features on the surface of this sample is approximately 0.27 ± 0.07 nm, which is slightly greater than for POPC/SM/Chol 75:2:23, but still not very pronounced. The width of the features is 28.87 ± 5.10 nm. The feature's heights and widths for all samples are summarized in Table 4.1.

The existence of pores in some of the samples does not have any bearing on conclusions regarding the topographical domain formation that are outlined in the Discussion section. However, the pores were an unexpected observation and therefore warrranted some additional attention. The Appendix section summarizes the statistical analysis and its results performed in order to determine the approximate size of the pores (length and width) and how much of the sample area they occupy.

---

[1] Please note that the bright high areas in Figure 4.10e are just an artifact of imaging and do not represent the real sample topography.

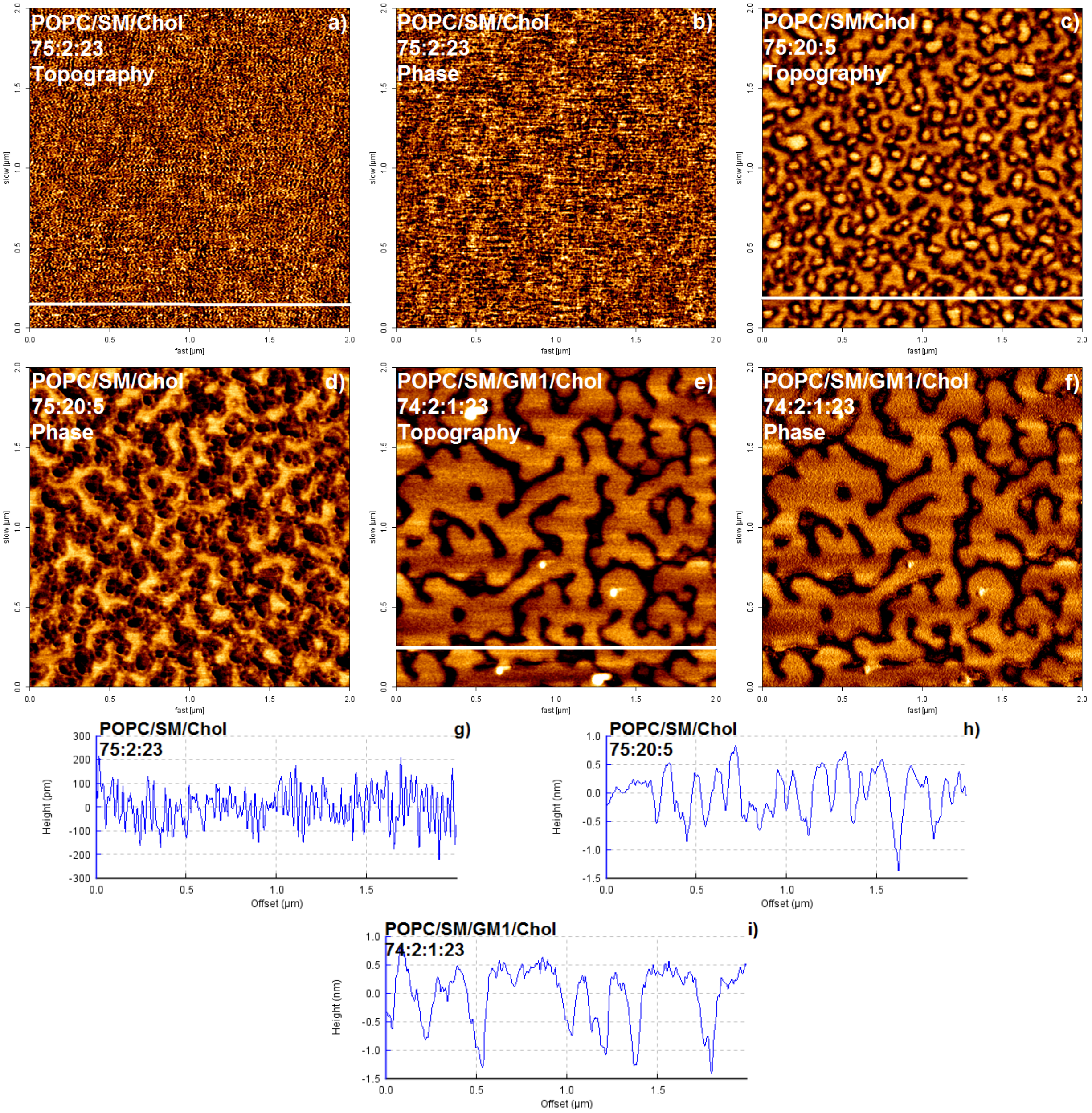

Figure 4.10: The AFM images (topographical, phase and cross-section) of the POPC/SM/Chol 75:2:23 (a, b, g), POPC/SM/Chol 75:20:5 (c, d, h) and POPC/SM/GM1Chol 74:2:1:23 (e, f, i), respectively.

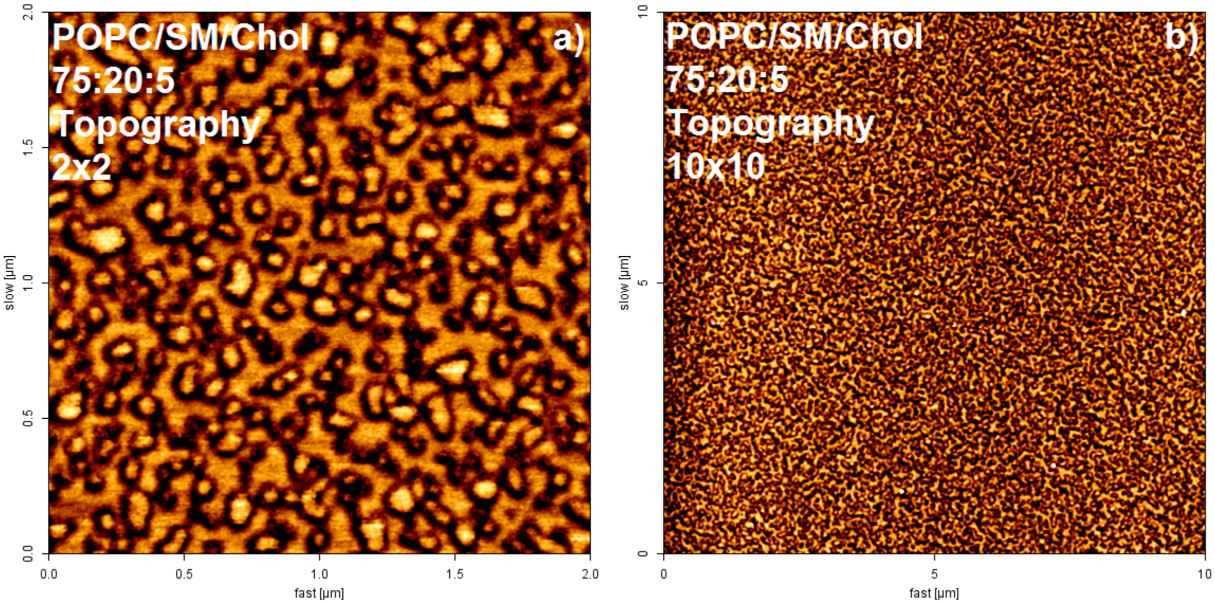

Figure 4.11: The comparison between $2\mu m \times 2\mu m$ (a) and $10\mu m \times 10\mu m$ (b) AFM images of POPC/SM/Chol 75:20:5.

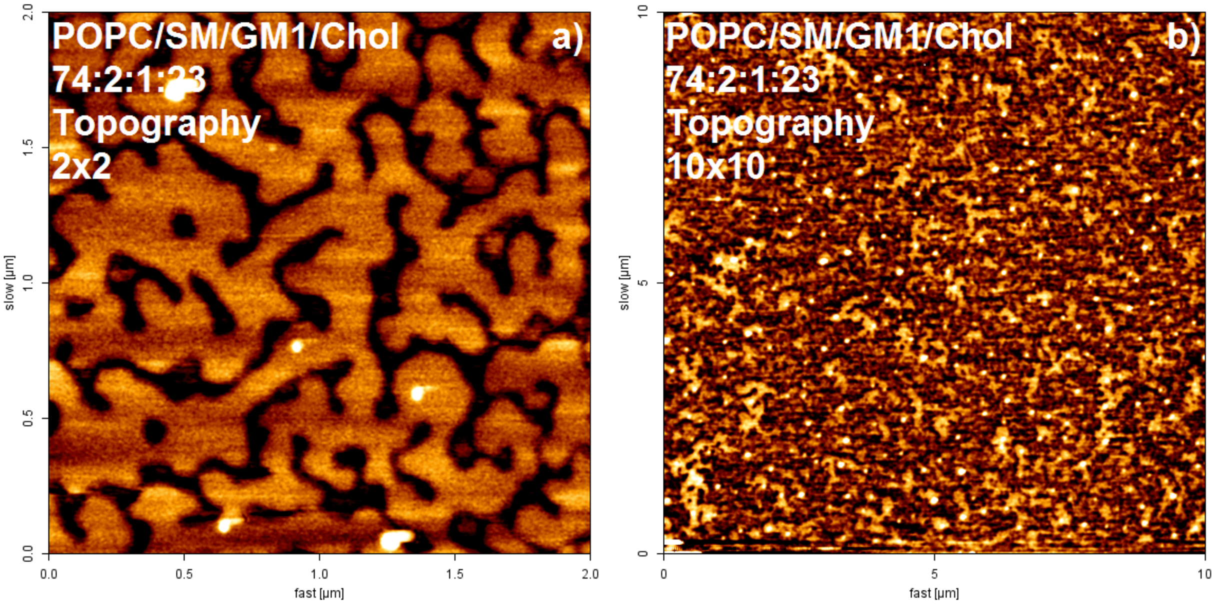

Figure 4.12: The comparison between $2\mu m \times 2\mu m$ (a) and $10\mu m \times 10\mu m$ (b) AFM images of POPC/SM/GM1/Chol 74:2:1:23.

Table 4.1: The list of heights and widths of observed topographical features, respectively.

Sample	Height (nm)	Width (nm)
POPC	0.21 ± 0.10	32.35 ± 11.06
POPG	0.36 ± 0.14	69.25 ± 14.32
POPC +20%	0.17 ± 0.07	35.81 ± 14.78
POPG +20%	0.20 ± 0.18	27.77 ± 8.51
POPC/POPG 60:40	0.26 ± 0.08	61.28 ± 9.88
POPC/POPG 60:40+5%Chol	0.36 ± 0.09	64.51 ± 11.93
POPC/POPG 60:40+20%Chol	0.26 ± 0.07	28.30 ± 7.42
POPC/POPG/SM 40:40:20	0.21 ± 0.05	36.68 ± 6.33
POPC/POPG/SM 40:40:20+5%Chol	0.58 ± 0.15	69.79 ± 10.07
POPC/POPG/SM 40:40:20+20%Chol	-	-
POPC/SM/Chol 75:2:23	0.16 ± 0.06	30.60 ± 4.46
POPC/SM/Chol 75:20:5	0.61 ± 0.12	63.21 ± 12.24
POPC/SM/GM1/Chol 74:2:1:23	0.27 ± 0.07	28.87 ± 5.10

4.6 Discussion

4.6.1 Pore Formation

The pore formation in 6 of the samples (see Table 6.1) was a very unexpected observation. There could be several explanations for the occurrence of this experimental artifact. The pores could be caused by defects in the mica surface that could result from uneven removal of cations from the surface while cleaving it. This would produce an uneven charge distribution on the surface and, as such, repel the lipids in places that are seen as pores on the images.

A charge on lipids could potentially impede their adsorption to mica, causing pores.

However, I do not believe this to be the case for my results. According to [82], mica carries a negative charge in an aqueous solution. The only charge lipid that I am using in this project is POPG, which also carries a negative charge. The repulsion between POPG and mica can explain the pore formation for the case of pure POPG and POPC/POPG 60:40 +5%Chol, but those are not the instances when the more prominent pores are observed. On the contrary, among the porous samples, the ones containing POPG exhibit smaller and shallower pores than most. If charge (on mica or lipid) is what's causing the pores, then that could potentially be solved by modifying the mica surface to promote binding or adding cations into solution to act as intermediates, as suggested in [82]. The pores could also be due to the presence of both positive and negative charges on the head group of POPC and SM (see Figure 3.1). The polarity of the head groups could be interfering with adsorption to mica surface.

Another hypothesis for the pore formation stems from the structure of POPC and POPG (see Figure 3.1). Both these lipids have a double bond in one the middle of one of their tail chains. This bond creates a kink in the tail. It is possible that this kink is interfering with the packing and mixing of the lipids creating the pores in monolayers even before their are transferred to mica. If that is the case and structure is what's causing the pores, then that could explain why the bigger and more pronounced pores are observed in the POPC/SM/GM1/Chol 74:2:1:23 sample. GM1 is the biggest species I use in the project. It could be that the bulk of GM1 prevents it from mixing well with the rest of the sample lipids in the mixture. This is supported by the fact that the pores appear to be unevenly distributed in the $10\mu m \times 10\mu m$ shown in Figure 4.12.

It appears though that addition of approximately 20% of Chol solves the pore formation issue, whether by facilitating the lipid adsorption to mica or by inducing more order and promoting mixing, or possible for some other reason that I have not considered. This, however, poses a problem for the goal of my project - addition of so much Chol does not seem to result in formation of well-defined domains. In order to reduce the occurrence of pores, it could be beneficial to attempt this experiment with model bilayers instead of monolayers. If it is the adsorption issue, then with a bilayer only one of its leaflets is attached to mica, leaving the other one free. Another possibility is to use graphite as the substrate, rather than mica. Graphite is hydrophobic and will have the non-polar tails adsorb to it, not the polar heads that could be causing mica-adsorption problem. Using graphite, though, presents a number of drawbacks: the head groups will have to be in solution so that the imaging could not be done in air, which will increase the difficulty level and required time for imaging.

4.6.2 Model Membrane

The POPC/SM/Chol 75:2:23 mixture follows the lipid proportions of neuronal cells found in a mouse[49]. However, for the purposes of studying the effect of surface heterogeneity on Aβ behavior this sample cannot be used, since it exhibits some of the smaller domains observed. After performing an additional literature search it was found that the level of SM in cell membranes tends to increase during the progress of Alzheimer's Disease (AD)[9, 108]. Unfortunately, it was not possible to determine the percentage value of this increase. This information, combined with the observation of formation of higher domains in previous samples with addition of 5%Chol, leads to the change in proportions in the new POPC/SM/Chol 75:20:5 mixture. I believe it is possible to use this mixture in further Aβ studies as a model for neuronal membrane at the end of the AD course. However, it is my opinion that an even better model for diseased membrane is the POPC/POPG/SM 40:40:20+5%Chol sample. The topographical features that this sample exhibits are slightly more pronounced than those of POPC/SM/Chol 75:20:5, with the domains being more well-defined and greater in width (see Table 4.1). It has been shown that POPG is important in Aβ binding to the membrane surface[14], therefore it should be present in a model that is used to investigate this process.

GM1 was added to the original POPC/SM/Chol 75:2:23 sample because it is a well-known component of neuronal membrane[6, 8, 27, 49, 61]. Additionally, the level of GM1 tends to decrease until it disappears as AD progresses[8, 27], therefore GM1 was not included into the POPC/SM/Chol 75:20:5 sample. As such, the POPC/SM/GM1/Chol

74:2:1:23 can be used as a model for the neuronal membrane in the early states of AD. Similarly, the original mixture of POPC/SM/Chol 75:2:23 can also be used as a model for healthy membrane. As a possible next step to this project, I believe it would be beneficial to slightly change the proportions in this sample so that they maintain the trend but also reflect the fact that such quantities of Chol do not produce very pronounced domains. This would mean lowering the amount of Chol and increasing the amount of SM. It could also be interesting to add GM1 into the diseased-membrane model (POPC/SM/Chol 75:20:5 or POPC/POPG/SM 40:40:20+5%Chol) in reduced quantities to simulate the effect of GM1 content decrease during AD.

The hypothesis of increased topographical features during the progress of AD is confirmed with the model membranes developed during this project. The two compositions that can represent healthy membrane (POPC/SM/Chol 75:2:23 and POPC/SM/GM1/Chol 74:2:1:23) exhibit topographical features that are not very pronounced, while the two compositions that model diseased membrane (POPC/SM/Chol 75:20:5 and POPC/POPG/SM 40:40:20+5%Chol) possess a strong topographical heterogeneity with large and well-defined domains (see Table 4.1).

This project was an attempt at modeling neuronal membrane, however, a lot of things were not taken into account. Due to the time constraints, only a few lipids and their combinations could be studied, but these lipids are by no means the sole constituents of a true cellular membrane. The lipids included here were deemed to be the most important ones in relation to membrane composition and Aβ-membrane interactions. I believe that, should a further study be undertaken, other lipids should be included. Among these potential additions is POPE (a less-prominent membrane component[60, 61]) and a number of other gangliosides (GM3, GD1a, GD1b[6, 8, 27, 61]) that have been implicated in Aβ behavioral mechanisms. Another matter that was not taken into account, due to being outside the scope of this investigation, is the fact that AD does not affect all areas of the brain equally and not all areas of the brain have the same types of neurons[8, 9, 61, 108]. Therefore it is impossible to come up with a generic model that could simulate all neuronal membranes. It would be of great benefit for future AD research if separate specialized models could be developed.

Chapter 5

Conclusion

This was a preliminary study with the purpose of determining a suitable model for a neuronal cell membrane that could later be used to investigate the effects of topographical heterogeneity on the binding and subsequent behavior of Aβ, a protein heavily implicated in the pathogenesis of Alzheimer's Disease (AD). Several samples composed of lipids usually found in neuronal membrane were tested during the course of the study, but very few of them exhibited any kind of domain (feature) formation.

The study revealed that a number of the mixtures do not bind well to mica resulting in formation of pores in the sample, which means that either a more suitable substrate or configuration (e.g. bilayer) need to be considered.

This project confirmed the hypothesis that topography of a cell membrane changes due to AD. The healthy membrane presents a smooth topography with small features, while a diseased membrane exhibits pronounced topographical domains that are bigger than the structures in the healthy membrane. A suitable model for a cell membrane composition during the early onset of AD is POPC/SM/GM1/Chol 74:2:1:23. The composition of this sample was modeled based on a study of a mouse brain composition, with GM1 being added to represent its presence in human neuronal membranes. This sample demonstrated potential for domain formation, which could probably be improved by slightly varying the proportions of SM and Chol. A more advanced stage of AD can be represented by either

POPC/SM/Chol 75:20:5 or POPC/POPG/SM 40:40:20+5%Chol mixtures. Both of these samples exhibit heterogeneous topography and have a higher SM content, consistent with published findings regarding SM level increase during AD. These samples do not include GM1 in their composition due to GM1 not being present in membranes during further stages of AD.

These three samples represent a very crude basic model that can provide a stepping stone in the studies of Aβ behavior. However, it is my strong belief that more work is required to develop a more accurate model for a neuronal membrane. Such a model should potentially account for the presence of other components not included here (such as other gangliosides, for example). A more sophisticated model should also not overlook the presence and role of proteins in a membrane, as well as, account for possible differences in composition of inner and outer leaflets of a bilayer membrane.

In conclusion, during my study I determined three possible basic models for a neuronal membrane at different stages of AD, but a more comprehensive study is required should a more complex model be needed.

Chapter 6

Appendix

The purpose of this Appendix is to illustrate the step-by-step process performed during statistical analysis of the AFM images using SPIP software. This analysis was done to determine the dimensions of the pores observed in six samples, see Table 4.1. The processing of images is largely subjective and depends on an individual's opinion about which function produces the "best-looking" image possible. In order to eliminate some of the subjectivity, I used the same procedure for all of my images.

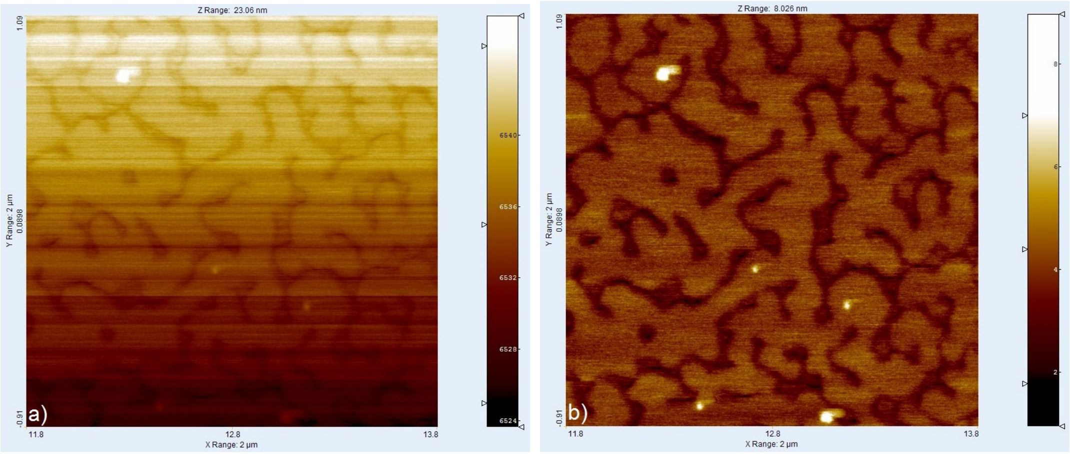

Figure 6.1: A .jpk image before (a) and after (b) plane correction.

The first step in any AFM image processing is a plane correction. It is designed to eliminate unwanted tilt in the image caused by non-linear coupling between the lateral plane and the Z-axis[110]. Figure 6.1a shows what the raw .jpk image looks like before any processing is done on it. I chose to do a Line-wise Correction, LMS Fit of Degree 2. An example of the image with this correction applied to it is given in Figure 6.1b.

Next, I adjusted the z-range to exclude the bright features that are seen in Figure 6.1b. These features are an artifact of imaging and do not represent the real topography of the sample, therefore, I wanted to eliminate them from being included in any further analysis. This process is shown in Figure 6.2.

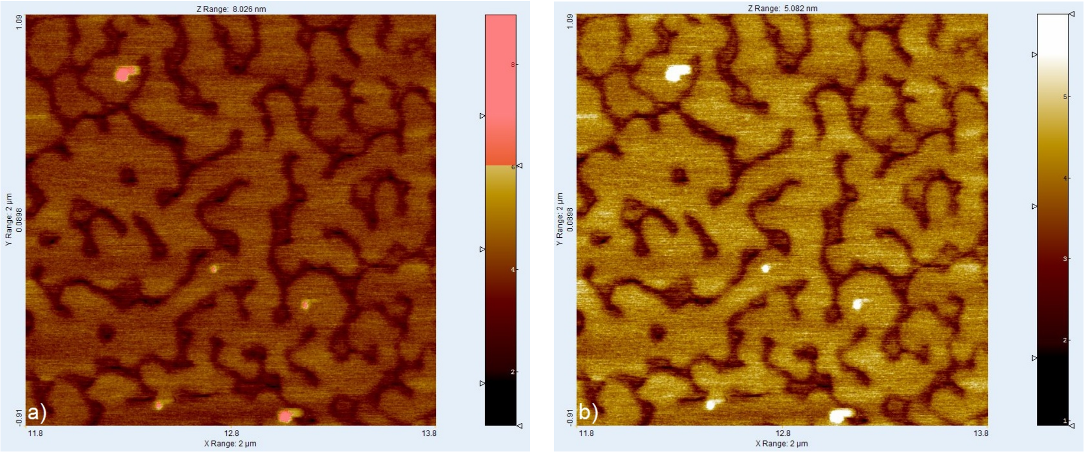

Figure 6.2: The z-correction of image to eliminate unwanted features. a) Selecting the features that need to be excluded. b) The image after the features are excluded. Note the change in the z-range.

In order to determine the average depth of pores and to find the percentage of area covered by them I used the Histogram function. The height histogram for the image in previous figures is given in Figure 6.3. Once the histogram was generated I used the cursor function to select two values (M1 and M2), the difference between which would be the depth value of the pores, shown in Figure 6.4. I found the depth values purely for the purposes of checking if they agreed with those obtained using a different method of analysis that produced values in Table 4.1. The SPIP generated values are listed in Table 6.1 and appear to be in agreement with those from Table 4.1.

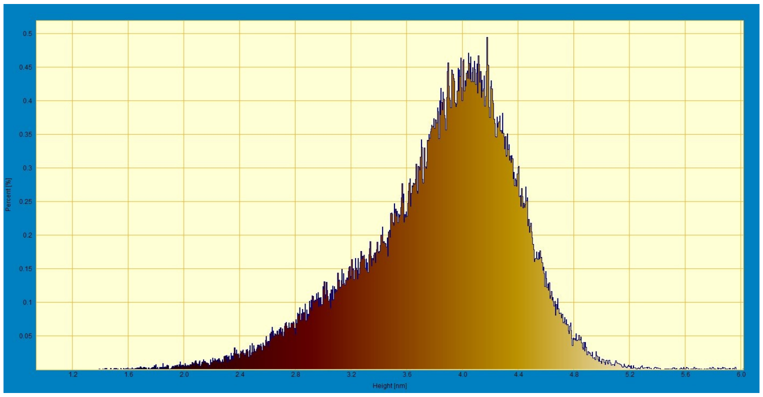

Figure 6.3: The histogram of height values distribution for the same image as in previous figures.

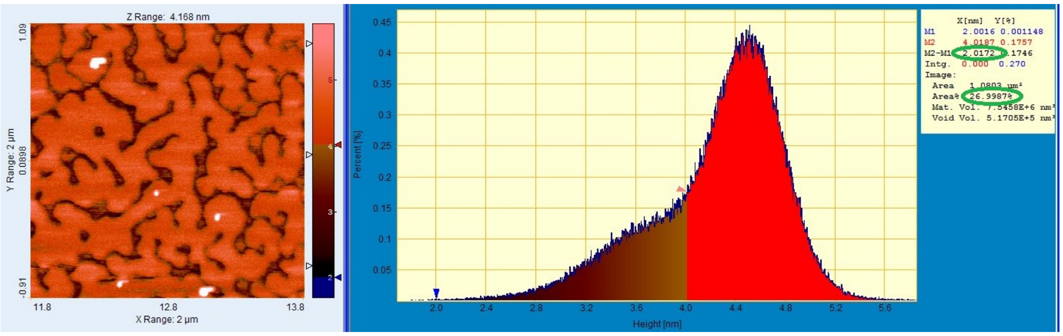

```
          X[nm]   Y[%]
M1       2.0016 0.001148
M2       4.0187 0.1757
M2-M1    2.0172 0.1746
Intg.    0.000  0.270
Image:
  Area    1.0803 um²
  Area%  26.9987%
  Mat. Vol. 7.5458E+6 nm³
  Void Vol. 5.1705E+5 nm³
```

Figure 6.4: Using the cursor function to select the range of desired heights. The resultant depth and area coverage measurement are circled in green.

The six samples that exhibit pore formation were then subjected to further analysis. Their features were well-defined enough for me to use Particle and Pore (P&P) analysis on them to determine the dimensions of the pores. However, there was still much noise in the samples, which interfered with the P&P analysis. In order to eliminate the noise I used the Gaussian smoothing function with standard deviation of 1. The benefit of Gaussian smoothing is illustrated in Figure 6.5, which shows the sample and its cross-section before and after smoothing.

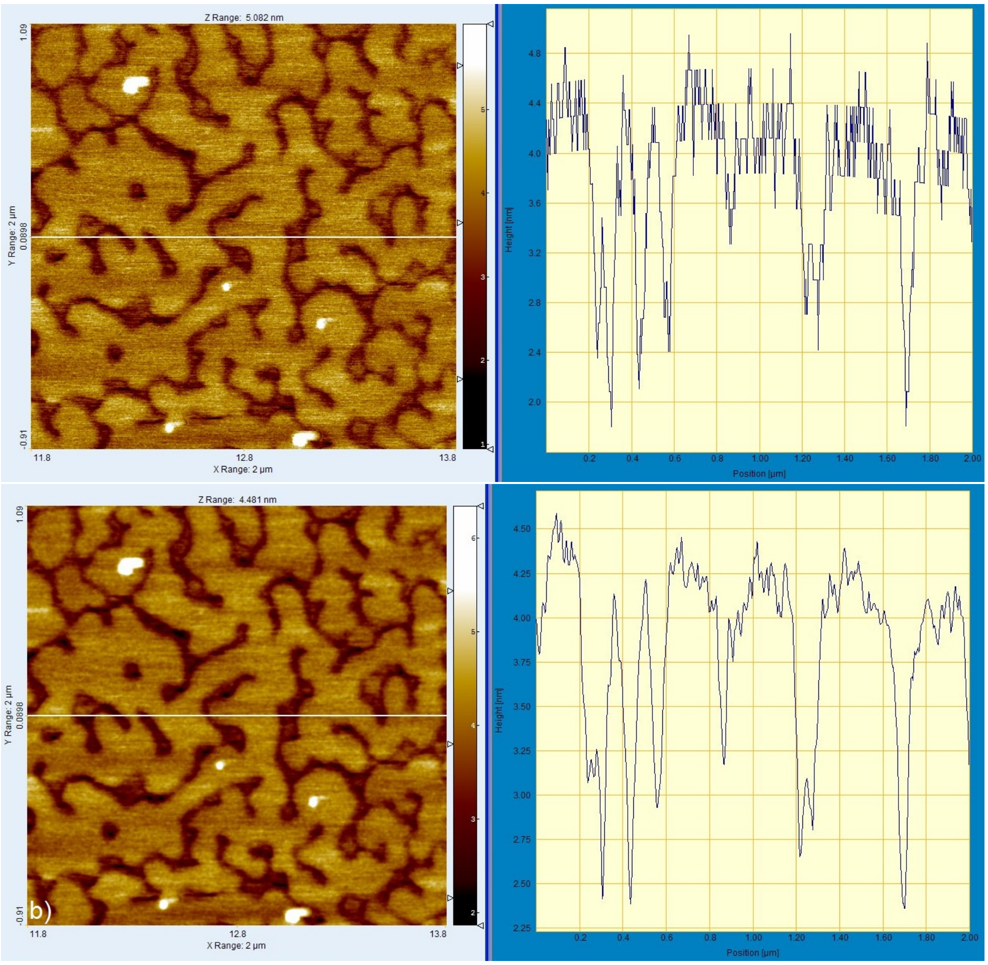

Figure 6.5: The sample and its cross-section before (a) and after (b) Gaussian smoothing.

After the image was smoothed, I was able to use the P&P analysis. I used Advanced Threshold option with Automatic detection (to minimize the subjectivity in selecting the threshold). An example of pore detection is given in Figure 6.6. This option allowed me to find an average value for the length and width (breadth) of the pores. It is important to note that the length and width are not the x- and y-dimensions of the pores. For a given pore, the software calculates these values based on the axis of momentum[110], as shown in Figure 6.7.

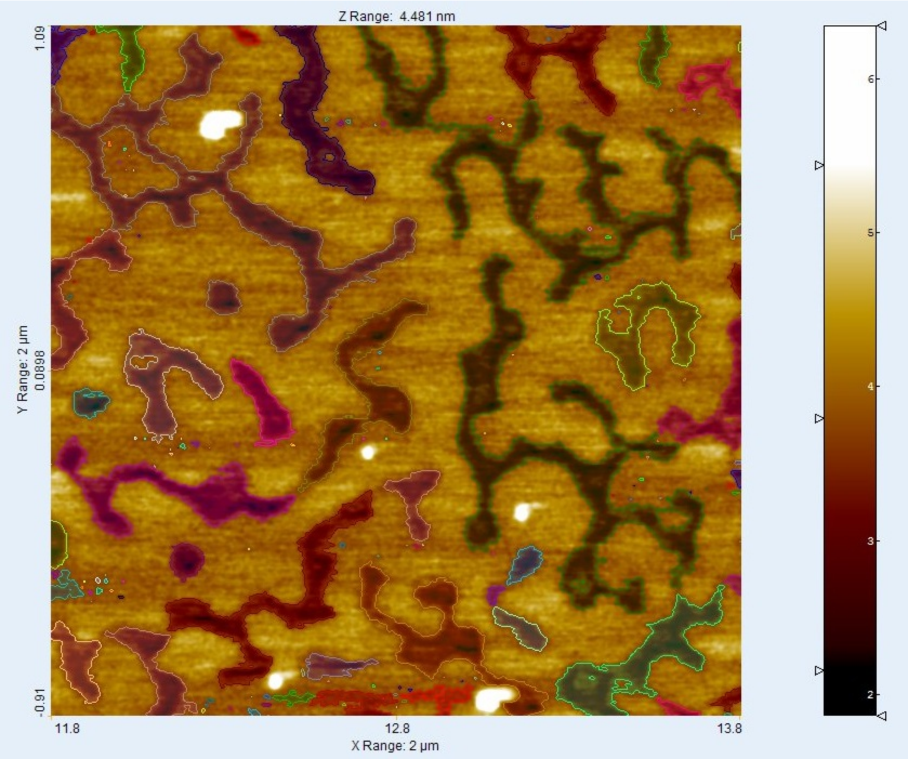

Figure 6.6: The Particle and Pore analysis function detecting the pores in the sample.

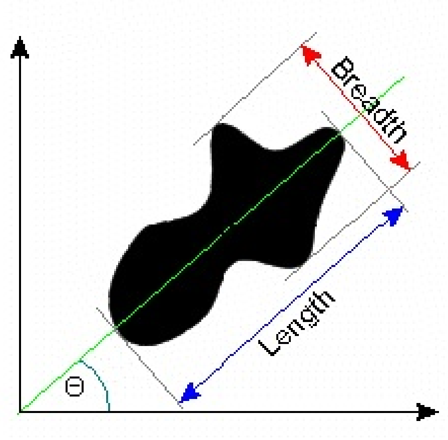

Figure 6.7: An illustration of the meaning of length and width in the SPIP software[110].

The pores in the control samples of POPC were found to cover $8.10 \pm 2.52\%$ of the sample area, which corresponds to 0.32 ± 0.10 μm^2 for a 2μm × 2μm image. In POPG samples the pores occupy a smaller area of $4.28 \pm 3.15\%$, which corresponds to 0.17 ± 0.13

μm^2 for a 2μm × 2μm image. However, the POPG pores showed a greater variability in how much area they occupy from image to image, which is reflected in the large value for standard deviation. The POPG pores were also found to be shallower (in agreement with the values quoted in the Results section) and smaller in size, as can be seen from Table 6.1.

The pores observed for the POPC/POPG 60:40+5%Chol sample appear to occupy a greater area than those of POPC or POPG with the coverage of 10.81 ± 4.82 % (0.43 ± 0.19 μm^2 for a 2μm × 2μm image). These pores also exhibited an uneven distribution resulting in the larger standard deviation value.

In case of the POPC/POPG/SM 40:40:20+5%Chol sample the pores were found to cover 25.11 ± 8.59% or 1.00 ± 0.34 μm^2 for a 2μm × 2μm image. This represents one of the worst cases of pore coverages observed during the project. The average length and width of the pores are also one of the greatest in all samples, as seen in Table 6.1. The large uncertainty values are a result of the pores all being of different sizes, with length and width varying between approximately 130 nm to 40 nm and 90 nm to 25 nm, respectively.

The pores in the POPC/SM/Chol 75:20:5 sample cover 12.60 ± 5.29% of the area, which corresponds to 0.50 ± 0.21 μm^2 for a 2μm × 2μm image. Similarly to POPC/POPG/SM 40:40:20+5%Chol, the large uncertainty values for the pore dimensions (see Table 6.1) result from the pores being of inconsistent size ranging from approximately 140 nm to 18 nm in length and 87 nm to 11 nm in width. Same variability in sizes is also seen in the POPC/SM/GM1/Chol 74:2:1:23 sample. The pores here occupy the largest area of all samples with a coverage of 26.28 ± 5.63% or 1.05 ± 0.23 μm^2 for a 2μm × 2μm image.

All of the above results are summarized in Table 6.1, along with the depth values found using the SPIP. These values appear to be in agreement with those quoted in the Results section (see Table 4.1). This analysis was performed in an attempt to characterize the pores observed in six of the samples. I would like to reiterate that the image analysis carries in it a lot of inherent subjectivity. Therefore the values quoted here should be viewed as approximate and not absolute.

Table 6.1: Dimensions of the pores observed in all the samples investigated in this study. The area column lists the % of sample area covered by the pores.

Sample	Depth (nm)	Area (%)	Length (nm)	Width (nm)
POPC	2.14 ± 0.15	8.10 ± 2.52	53.56 ± 3.55	36.05 ± 2.75
POPG	1.11 ± 0.23	4.28 ± 3.15	36.19 ± 5.09	20.91 ± 3.03
POPC +20%	-	-	-	-
POPG +20%	-	-	-	-
POPC/POPG 60:40	-	-	-	-
POPC/POPG 60:40+5%Chol	-	-	-	-
POPC/POPG 60:40+20%Chol	-	-	-	-
POPC/POPG/SM 40:40:20	-	-	-	-
POPC/POPG/SM 40:40:20+5%Chol	1.37 ± 0.27	25.11 ± 8.59	85.48 ± 40.84	53.02 ± 27.37
POPC/POPG/SM 40:40:20+20%Chol	-	-	-	-
POPC/SM/Chol 75:2:23	-	-	-	-
POPC/SM/Chol 75:20:5	1.41 ± 0.14	12.60 ± 5.29	68.86 ± 51.98	40.33 ± 30.40
POPC/SM/GM1/Chol 74:2:1:23	2.15 ± 0.61	26.28 ± 5.63	94.44 ± 35.09	50.98 ± 18.07

References

[1] I. Peters et al. The interaction of beta-amyloid protein with cellular membranes stimulates its own production. *Biochimica et Biophysica Acta*, 1788(5):964–972, 2009.

[2] A. Choucair et al. Preferential accumulation of aβ(142) on gel phase domains of lipid bilayers: An AFM and fluorescence study. *Biochimica et Biophysica Acta*, 1768:146154, 2007.

[3] E.Terzi, G. Holzemann, and J. Seelig. Interaction of Alzheimer β-amyloid peptide(1-40) with lipid membranes. *Biochemistry*, 36:14845–14852, 1997.

[4] L. Qiu et al. Cholesterol modulates the interaction of β-amyloid peptide with lipid bilayers. *Biophysical Journal*, 96:42994307, 2009.

[5] K. Matsuzaki. Physiochemical interactions of amyloid β-peptide with lipid bilayers. *Biochimica et Biophysica Acta*, 1768:19351942, 2007.

[6] G. Di Paolo and T.-W. Kim. Linking lipids to Alzheimer's disease: cholesterol and beyond. *Nature Reviews Neuroscience*, 12:284–296, 2011.

[7] J. V. Rushworth and N. M. Hooper. Lipid rafts: linking Alzheimer's amyloid-β production, aggregation, and toxicity at neuronal membranes. *International Journal of Alzheimer's Disease*, 2011:1–14, 2011.

[8] T. Ariga, M. P. McDonald, and R. K. Yu. Role of ganglioside metabolism in the pathogenesis of Alzheimers diseasea review. *Journal of Lipid Research*, 49:1157–1175, 2008.

[9] X. He et al. Deregulation of sphingolipid metabolism in Alzheimers disease. *Neurobiology of Aging*, 31:398–408, 2010.

[10] M. Vestergaard, T. Hamada, and M. Takagi. Using model membranes for the study of amyloid beta: Lipid interactions and neurotoxicity. *Biotechnology and Bioengineering*, 99(4):424–429, 2008.

[11] F. Hane et al. Amyloid-β aggregation on model lipid membranes: An Atomic Force Microscopy study. *Journal of Alzheimer's Disease*, 25:110, 2011.

[12] H. Lin, R. Bhatia, and R. Lal. Amyloid β protein forms ion channels: implications for Alzheimer's disease pathophysiology. *The FASEB Journal*, 15:2433–2444, 2001.

[13] A. Chauhan, I. Ray, and V. P. S. Chauhan. Interaction of Amyloid beta-protein with anionic phospholipids: Possible involvement of Lys28 and C-terminus aliphatic amino acids. *Neurochemical Research*, 25:423429, 2000.

[14] S. M. Butterfield and H. A. Lashuel. Amyloidogenic protein-membrane interactions: mechanistic insight from model systems. *Angewandte Chemie International Edition*, 49:5628–5654, 2010.

[15] S. Varadarajan et al. Review: Alzheimer's amyloid β-peptide-associated free radical oxidative stress and neurotoxicity. *Journal of Structural Biology*, 130:184–208, 2000.

[16] Ch-S. Wanga, R.J. Wurtmana, and R. K. K. Leeb. Amyloid precursor protein and membrane phospholipids in primary cortical neurons increase with development, or after exposure to nerve growth factor or aβ_{1-40}. *Brain Research*, 865:157167, 2000.

[17] J. N. Kanfer, G. Sorrentino, and D. S. Sita. Amyloid beta peptide membrane perturbation is the basis for its biological effects. *Neurochemical Research*, 24(12):1621–1630, 1999.

[18] S. Bodovitz and W. L. Klein. Cholesterol modulates α-secretase cleavage of amyloid precursor protein. *The Journal of Biological Chemistry*, 271(8):4436–4440, 1996.

[19] E. Drolle et al. Nanoscale electrostatic domains in Cholesteral-laden lipid membranes create a target for Amyloid binding. *Biophysical Journal*, 103:L27–L29, 2012.

[20] V. Koppaka and P. H. Axelsen. Accelerated accumulation of Amyloid β proteins on oxidatively damaged lipid membranes. *Biochemistry*, 39:10011–10016, 2000.

[21] E. Y. Chi, S. L. Frey, and K. Y. C. Lee. Ganglioside G_{M1}-mediated amyloid-beta fibrillogenesis and membrane disruption. *Biochemistry*, 46:1913–1924, 2007.

[22] A. Kakio et al. Cholesterol-dependent formation of GM1 ganglioside-bound Amyloid β-protein, an endogenous seed for Alzheimer Amyloid. *The Journal of Biological Chemistry*, 276:24985–24990, 2001.

[23] I. Benilova, E. Karran, and B. De Strooper. The toxic Aβ oligomer and Alzheimers disease: an emperor in need of clothes. *Nature Neuroscience*, 15(3):349–357, 2012.

[24] P. K. J. Kinnunen. Amyloid formation on lipid membrane surfaces. *The Open Biology Journal*, 2:163–175, 2009.

[25] M. O. W. Grimm et al. Regulation of cholesterol and sphingomyelin metabolism by amyloid-β and presenilin. *Nature Cell Biology*, 7(11):1118–1123, 2005.

[26] A.V. Maltseva, S. Bystryak, and O.V. Galzitskaya. The role of β -amyloid peptide in neurodegenerative diseases. *Ageing Research Reviews*, 10:440–452, 2011.

[27] J. Fantini and N. Yahi. Molecular insights into amyloid regulation by membrane cholesterol and sphingolipids: common mechanisms in neurodegenerative diseases. *Expert Reviews in Molecular Medicine*, 12(27):1–22, 2010.

[28] J. D. Green et al. Atomic force microscopy reveals defects within mica supported lipid bilayers induced by the amyloidogenic human amylin peptide. *The Journal of Molecular Biology*, 342:877–887, 2004.

[29] P. Nelson. In *Biological Physics: Energy, Information, Life. Updated First Edition.* W. H. Freeman and Company, 2008.

[30] S. J. Singer and G. L. Nicolson. The fluid mosaic model of the structure of cell membranes. *Science*, 175:720–731, 1972.

[31] R. M. A. Sullan. In *Nanomechanics of Barnacle Proteins and Multicomponent Lipid Bilayers Studied by Atomic Force Microscopy.* Graduate Department of Chemistry, University of Toronto, Library and Archives Canada, 2010.

[32] P. Atkins and J. de Paula. In *Atkin's Physical Chemistry, 8th ed.* W. H. Freeman and Company, 2006.

[33] C. Gimnez. Composition and structure of the neuronal membrane: molecular basis of its physiology and pathology. *Revista de Neurologa*, 26(150):232–239, 1998.

[34] J. M. Berg, J. L. Tymoczko, and L. Stryer. In *Biochemistry. 5th edition.* W. H. Freeman and Company, 2002.

[35] V. J. Morris, A. R. Kirby, and A. P. Gunning. In *Atomic Force Microscopy for Biologists.* Imperial College Press, 1999.

[36] Amphipathic molecules and phospholipid bilayers. `http://www.freethought-forum.com/forum/showthread.php?t=24978&garpg=6`, 2011.

[37] O. Coban et al. Transition from nanodomains to microdomains induced by exposure of lipid monolayers to air. *Biophysical Journal*, 92:2842–2853, 2007.

[38] C. Yuan et al. The size of lipid rafts: an atomic force microscopy study of ganglioside GM1 domains in sphingomyelin/DOPC/cholesterol membranes. *Biophysical Journal*, 82:2526–2535, 2002.

[39] What keeps a phospholipid bilayer of one cell from fusing with the bilayer of another cell? http://www.quora.com/What-keeps-a-phospholipid-bilayer-of-one-cell-from-fusing-with-the-bilayer-of-another-cell, 2011.

[40] K. Simons and W. L. C. Vaz. Model systems, lipid rafts, and cell membranes. *Annual Review of Biophysics and Biomolecular Structure*, 33:269–295, 2004.

[41] Inc. Avanti Polar Lipids. 16:0 PC (DPPC). http://avantilipids.com/index.php?option=com_content&view=article&id=216&Itemid=206&catnumber=850355.

[42] Inc. Avanti Polar Lipids. 18:1 (Δ9-Cis) PC (DOPC). http://avantilipids.com/index.php?option=com_content&view=article&id=231&Itemid=207&catnumber=850375.

[43] J. F. Thompson. Fluid mosaic model. http://apbrwww5.apsu.edu/thompsonj/Anatomy%20&%20Physiology/2010, 2010.

[44] C. Yuan and L. J. Johnston. Distribution of ganlioside GM1 in L-α-dipalmitoylphosphatudylcholine/cholesterol monolayers: a model of lipid rafts. *Biophysical Journal*, 79:2768–2781, 2000.

[45] G. Oradd, P. W. Westerman, and G. Lindblom. Lateral diffusion coefficients of separate lipid species in ternary raft-forming bilayer: a Pfg-NMR multinuclear study. *Biophysical Journal*, 89:315–320, 2005.

[46] H. A. Rinia et al. Visualizing detergent resistant domains in model membranes with atomic force microscopy. *FEBS Letters*, 501:92–96, 2001.

[47] E. Londonl. Insights into lipid raft structure and formation from experiments in model membranes. *Current Opinion in Structural Biology*, 12:480–486, 2002.

[48] R. F. M. de Almeida et al. Lipid rafts have different sizes depending on membrane composition: a time-resolved fluorescence resonance energy transfer study. *The Journal of Molecular Biology*, 346:1109–1120, 2005.

[49] F. Scandroglio et al. Lipid content of brain, of brain membrane lipid domains, and of neurons from acid sphingomyelinase deficient mice (ASMKO). *Journal of Neurochemistry*, 107(2):329–338, 2008.

[50] M. Edidin. The state of lipid rafts: from model t membranes to cells. *Annual Review of Biophysics and Biomolecular Structure*, 32:257–283, 2003.

[51] B. Y. van Duyl et al. Sphingomyelin is much more effective than saturated phosphatidylcholine in excluding unsaturated phosphatidylcholine from domains formed with cholesterol. *FEBS Letters*, 547:101–106, 2003.

[52] S. A. Pandit, E. Jakobsson, and H. L. Scott. Simulation of the early stages of nano-domain formation in mixed bilayers of sphingomyelin, cholesterol and dioleylphosphatidylcholine. *Biophysical Journal*, 87:3312–3322, 2004.

[53] I. E. Andras, S. Y. Eum, and M. Toborek. Lipid rafts and functional caveolae regulate HIV-induced amyloid beta accumulation in brain endothelial cells. *Biochemical and Biophysical Research Communications*, 421:177–183, 2012.

[54] L. A. Lopez et al. Anti-tetherin activities of HIV-1 Vpu and ebola virus glycoprotein do not involve removal of tetherin from lipid rafts. *Journal of Virology*, 86(10):5467–5480, 2012.

[55] R. V. Bowie et al. Lipid rafts are disrupted in mildly-inflamed intestinal microenvironments without overt disruption of the epithelial barrier. *American Journal of Physiology*, In press, doi: 10.1152/ajpgi.00002.2011, 2012.

[56] H.-C. Lin et al. Fas ligand enhances the malignant behavior of tumor cells through interaction with Met, hepatocyte growth factor receptor, in lipid rafts. *The Journal of Biological Chemistry*, In press, doi: 10.1074/jbc.M111.326058, 2012.

[57] G. Dawson et al. Abnormal gangliosides are localized in lipid rafts in sanfilippo (MPS3a) mouse brain. *Neurochemical Research*, 37:1372–1380, 2012.

[58] F. Tokumasu et al. Nanoscopic lipid domain dynamics revealed by atomic force microscopy. *Biophysical Journal*, 84:2609–2618, 2003.

[59] W-C. Lin et al. Lipid asymmetry in DLPC/DSPC-supported lipid bilayers: a combined AFM and fluorescence microscopy study. *Biophysical Journal*, 90:228–237, 2006.

[60] I. Dreissig et al. Quantification of brain lipids by ftir spectroscopy and partial least squares regression. *Spectrochimica Acta Part A*, 71:2069–2075, 2009.

[61] R. O. Calderon, B. Attema, and G. H. DeVries. Lipid composition of neuronal cell bodies and neurites from cultured dorsal root ganglia. *Journal of Neurochemistry*, 64(1):424–429, 1995.

[62] G. W. Feigenson and J. T. Buboltz. Ternary phase diagram of dipalmitoyl-PC/dilauroyl-PC/cholesterol: nanoscopic domain formation driven by cholesterol. *Biophysical Journal*, 80:2775–2788, 2001.

[63] J. S. O'Brien and E. L. Sampson. Lipid composition of the normal human brain: gray matter, white matter, and myelin. *Journal of Lipid Research*, 6:537–544, 1965.

[64] E. R. Kandel, J. H. Schwartz, and T. M. Jessell. In *Principles of Neural Science, 4th ed.* McGraw-Hill, 2000.

[65] P. E. Milhiet et al. High-resolution AFM of membrane proteins directly incorporated at high density in planar lipid bilayer. *Biophysical Journal*, 91:3268–3275, 2006.

[66] K. S. Birdi and D. T. Vu. Structures of collapsed lipid monolayers investigated as Langmuir-Blodgett films by atomic force microscopy. *Langmuir*, 10:623–625, 1994.

[67] KSV Instruments Ltd. Langmuir and Langmuir-Blodgett films. `http://www.lot-oriel.com/files/downloads/ksv/en/langmuirblodgett_en01.pdf`.

[68] Nima Technology Ltd. Langmuit-Blodgett troughs: operating manual, 6th ed. `http://www.ksvnima.com/`, 2001.

[69] S. H. Maron and C. E. Prutton. In *Principles of Physical Chemistry, 3rd ed.* The MacMillan Company, 1959.

[70] C-K. Lee et al. Atomic force microscopy: Determination of unbinding force, off rate and energy barrier for proteinligand interaction. *Micron*, 38:446–461, 2007.

[71] G. Binnig, C. F. Quate, and Ch. Gerber. Atomic force microscope. *Physical Review Letters*, 56(9):930–933, 1986.

[72] Y. F. Dufrene. Application of atomic force microscopy to microbial surfaces: from reconstituted cell surface layers to living cells. *Micron*, 32:153–165, 2001.

[73] R. J. Colton et al. Scanning probe microscopy. *Current Opinion in Chemical Biology*, 1:370–377, 1997.

[74] P. Hinterdorfer and Y. F. Dufrene. Detection and localization of single molecular recognition events using atomic force microscopy. *Nature Methods*, 3(5):347–355, 2006.

[75] N. Hilal et al. A review of atomic force microscopy applied to cell interactions with membranes. *Chemical Engineering Research and Design*, 84(A4):282–292, 2006.

[76] L. A. Bottomley, J. E. Coury, and P. N. First. Scanning probe microscopy. *Analytical Chemistry*, 68:185R–230R, 1996.

[77] G. E. Xiaopeng et al. Afm study on the adsorption and aggregation behavior of dissolved humic substances on mica. *Science in China: Series B Chemistry*, 49(3):256–266, 2006.

[78] J. L. Alonso and W. H. Goldmann. Feeling the forces: atomic force microscopy in cell biology. *Life Sciences*, 72:2553–2560, 2003.

[79] K. Franze. Atomic force microscopy and its contribution to understanding the development of the nervous system. *Current Opinion in Genetics and Development*, 21:1–8, 2011.

[80] E. Meyer. Atomic force microscopy. *Progress in Surface Science*, 41:3–49, 1992.

[81] JPK instruments. The NanoWizard AFM Handbook. Version 1.2. `http://www.jpk.com/nanowizard-r-3-accessories.541.en.html`, 2005.

[82] N. C. Santos and M. A. R. B. Castanho. An overview of the biophysical applications of atomic force microscopy. *Biophysical Chemistry*, 107:133–149, 2004.

[83] JPK Instruments. NanoWizard II AFM. http://www.jpk.com/nanowizard-r-ii-overview.351.en.html.

[84] Veeco Metrology Group Digital Instruments. Scanning Probe Microscopy Training Notebook, Version 3.0, 2000.

[85] N. A. Geisse. Afm and combined optical techniques. *Materials Today*, 12:40–45, 2009.

[86] T. Ando, T. Uchihashi, and T. Fukuma. High-speed atomic force microscopy for nano-visualization of dynamic biomolecular processes. *Progress in Surface Science*, 83:337–437, 2008.

[87] Missouri Botanical Garden. Cantilevers and tips for SPM. http://www.mobot.org/jwcross/spm/cantilevers.htm, 2003.

[88] Aist-NT Inc. fpN11 Non-contact and Tapping Probe. http://nanoprobes.aist-nt.com/index.php?main_page=product_info&cPath=65&products_id=188&zenid=f0e1042b04b168186d9b5815d2faa403, 2012.

[89] S. Scheuring et al. Imaging streptavidin 2d crystals on biotinylated lipid monolayers at high resolution with the atomic force microscope. *Journal of Microscopy*, 193:28–35, 1999.

[90] A. Engel. Biological applications of scanning probe microscopes. *Annual Review of Biophysics*, 20:79–108, 1991.

[91] Q. Zhong and D. Inniss. Fractured polymer/silica fiber surface studied by tapping mode atomic force microscopy. *Surface Science Letters*, 290:L688–L692, 1993.

[92] D. R. Louder and B. A. Parkinson. Scanning probe microscopy. *Analytical Chemistry*, 66:84R–105R, 1994.

[93] K. R. Spring and M. W. Davidson for Nikon MicroscopyU. Introduction to fluorescence microscopy. http://www.microscopyu.com/articles/fluorescence/fluorescenceintro.html, 2012.

[94] D. A. Agard et al. Fluorescence microscopy in three dimensions. *Methods in Cell Biology*, 30:353–377, 1989.

[95] D. Vaknin, M. C. Kelley, and B. M. Ocko. Sphingomyelin at the airwater interface. *The Journal of Chemical Physics*, 115(16):7697–7704, 2001.

[96] T.-Y. Wang and J. R. Silvius. Different sphingolipids show differential partitioning into sphingolipid/cholesterol-rich domains in lipid bilayers. *Biophysical Journal*, 79:1478–1489, 2000.

[97] T.-Y. Wang and J. R. Silvius. Sphingolipid partitioning into ordered domains in cholesterol-free and cholesterol-containing lipid bilayers. *Biophysical Journal*, 84:367–378, 2003.

[98] D. A. Brown and E. London. Topical review: Structure and origin of ordered lipid domains in biological membranes. *The Journal of Membrane Biology*, 164:103–114, 1998.

[99] L. K. Bar, Y. Barenholz, and T. E. Thompson. Effect of sphingomyelin composition on the phase structure of phosphatidylcholine-sphingomyelin bilayers. *Biochemistry*, 36:2507–2516, 1997.

[100] J. M. Holopainen et al. Evidence for the lack of a specific interaction between cholesterol and sphingomyelin. *Biophysical Journal*, 86:1510–1520, 2004.

[101] J. E. Shaw et al. Correlated fluorescence-atomic force microscopy of membrane domains: Structure of fluorescence probes determines lipid localization. *Biophysical Journal*, 90:2170–2178, 2006.

[102] S. L. Veatch and S. L. Keller. Miscibility phase diagrams of giant vesicles containing sphingomyelin. *Physical Review Letters*, 94:148101(1)–148101(4), 2005.

[103] T. Baumgart et al. Fluorescence probe partitioning between Lo/Ld phases in lipid membranes. *Biochimica et Biophysica Acta*, 1768:2182–2194, 2007.

[104] T. Baumgart et al. Large-scale fluid/fluid phase separation of proteins and lipids in giant plasma membrane vesicles. *Proceedings of the National Academy of Sciences*, 104(9):3165–3170, 2006.

[105] I. A. Boldyrev et al. New BODIPY lipid probes for fluorescence studies of membranes. *Journal of Lipid Research*, 48:1518–1532, 2007.

[106] E. Drolle, PhD Candidate, University of Waterloo. Personal Communication, 2011-2012.

[107] R. F. M. de Almeida, A. Fedorov, and M. Prieto. Sphingomyelin/phosphatidylcholine/cholesterol phase diagram: boundaries and composition of lipid rafts. *Biophysical Journal*, 85:2406–2416, 2003.

[108] V. V. R. Bandaru et al. ApoE4 disrupts sterol and sphingolipid metabolism in Alzheimer's but not normal brain. *Neurobiology of Aging*, 30:591–599, 2009.

[109] JPK Instruments. The NanoWizard IP Image Processing Manual, Version 3.2, 2008.

[110] Image Metrology. Scanning Probe Image Processor User's Guide. `http://www.imagemet.com/WebHelp/spip.htm`.

[111] Inc. Avanti Polar Lipids. 16:0-18:1 PC. `http://www.avantilipids.com/index.php?option=com_content&view=article&id=243&Itemid=208&catnumber=850457`.

[112] Inc. Avanti Polar Lipids. 16:0-18:1 PG. `http://www.avantilipids.com/index.php?option=com_content&view=article&id=595&Itemid=235&catnumber=840457`.

[113] Inc. Avanti Polar Lipids. Sphingomyelin (d18:1/12:0). `http://www.avantilipids.com/index.php?option=com_content&view=article&id=1572&Itemid=581&catnumber=LM-2312`.

[114] Sigma-Aldrich Co. LLC. Cholesterol. http://www.sigmaaldrich.com/catalog/product/sigma/c8667?lang=en&region=CA.

[115] Inc. Avanti Polar Lipids. Ganglioside GM1 (Ovine Brain). http://www.avantilipids.com/index.php?option=com_content&view=article&id=442&Itemid=271&catnumber=860065.

[116] X. Zhang, Application Scientist, Biolin Scientific Inc. Communication via E-mail, 2012.

[117] L. Picas et al. Miscibility behavior and nanostructure of monolayers of the main phospholipids of *Escherichia coli* inner membrane. *Langmuir*, 28:701–706, 2012.

[118] D. Rose et al. Molecular dynamics simulations of lung surfactant lipid monolayers. *Biophysical Chemistry*, 138:67–77, 2008.

[119] N. Holten-Andersen et al. KL_4 peptide induces reversible collapse structures on multiple length scales in model lung surfactant. *Biophysical Journal*, 101:2957–2965, 2011.

[120] L. K. Tamm. Incorporation of a synthetic mitochondrial signal peptide into charged and uncharged phospholipid monolayers. *Biochemistry*, 25:7470–7416, 1986.

[121] A. Kouzayha and F. Besson. GPI-alkaline phosphatase insertion into phosphatidylcholine monolayers: Phase behavior and morphology changes. *Biochemical and Biophysical Research Communications*, 333:1315–1321, 2005.

[122] G. Thakur et al. Surface chemistry of lipid raft and amyliod Aβ (1-40) Langmuir monolayer. *Colloids and Surfaces B: Biointerfaces*, 87:369–377, 2011.

[123] M. Kepczynski et al. Interactions of a hydrophobically modified polycation with zwitterionic lipid membranes. *Langmuir*, 28:676–688, 2012.

[124] N. Kucerka et al. Scattering density profile model of POPG bilayers as determined by molecular dynamics simulations and small-angle neutron and x-ray scattering experiments. *The Journal of Physical Chemistry*, 116:232–239, 2012.